

Modeling the water masses of the Atlantic Ocean at the Last Glacial Maximum

André Paul and Christian Schäfer-Neth

DFG Research Center Ocean Margins, Department of Geosciences, University of Bremen, Germany

Received 11 March 2002; revised 12 December 2002; accepted 20 March 2003; published 9 July 2003.

[1] We produced gridded monthly sea-surface boundary conditions for the Atlantic Ocean at the Last Glacial Maximum (LGM) based on the sea-surface temperature reconstruction of the GLAMAP project. We used an ocean general circulation model (OGCM), subject to these sea-surface boundary conditions and a corresponding wind stress field from an atmospheric general circulation model, to study the differences in the distribution of the main water masses between the LGM and the present. Our global OGCM is characterized by high vertical resolution, low vertical diffusion, and isopycnal mixing and hence allows for a realistic representation of the hydrology and circulation of the modern Atlantic Ocean. According to a series of LGM experiments with an increasing sea-surface salinity anomaly in the Weddell Sea, the ventilated thermocline was colder than today by 2–3°C in the North Atlantic Ocean and, in the experiment with the largest anomaly (1.0 beyond the global anomaly), by 4–5°C in the South Atlantic Ocean. Its depth was reduced by 50 m on average, most notably in the tropics. In the North Atlantic Ocean the outcrop locations of the thermocline isopycnal surfaces migrated southward by 5°–10°, and the ventilation increased. In the South Atlantic Ocean the mixed layer and thermocline water masses were dominated by cold water originating from Drake Passage, and the import of warm water from the Indian Ocean was reduced to about 4 Sv or 40% of its modern value. Antarctic Intermediate Water was colder by 3–4°C and could be traced as far as 10°N. The meridional overturning rates of North Atlantic Deep Water (NADW) and Antarctic Bottom Water (AABW) in the Atlantic Ocean were similar to those of the present-day experiment (9–10 Sv and 4 Sv, respectively). However, NADW cooled by 2.5°C and AABW by 1°C. AABW was near the freezing point of seawater at the surface and the saltiest water mass in the Atlantic Ocean, even saltier than NADW. We show that the differences between the LGM and the present-day experiments can be traced back to the changes in the subpolar and interhemispheric sea-surface density gradients.

INDEX TERMS: 4255 Oceanography: General: Numerical modeling; 4283 Oceanography: General: Water masses; 4870 Oceanography: Biological and Chemical: Stable isotopes; 9325 Information Related to Geographic Region: Atlantic Ocean; *KEYWORDS:* GLAMAP 2000, ocean modeling, Atlantic Ocean, Last Glacial Maximum (LGM), ventilated thermocline, interocean exchange

Citation: Paul, A., and C. Schäfer-Neth, Modeling the water masses of the Atlantic Ocean at the Last Glacial Maximum, *Paleoceanography*, 18(3), 1058, doi:10.1029/2002PA000783, 2003.

1. Introduction

[2] Paleoclimatic data are very important in further developing our insight into climate change because they put climate variations into a long-term perspective and document their full range. They give clues about how the climate system works and provide a target for testing theories and models [Hartmann, 1994].

[3] With respect to the present climatic conditions, the CLIMAP Project Members [1981] reconstruction of sea-surface temperature (SST) for the global ocean at the Last Glacial Maximum (LGM) shows a strong cooling and a large increase in sea-ice cover that are consistent with the high albedo of the huge Northern Hemisphere ice sheets, the low concentration of carbon dioxide in the atmosphere and the reduced sea level. According to this now classic reconstruction, the global mean SST was about 1.6°C lower than today, and the winter sea-ice cover in the North

Atlantic Ocean extended equatorward of 50°N. Sea ice around Antarctica was greatly expanded.

[4] As compared to CLIMAP, the GLAMAP (Glacial Atlantic Ocean Mapping) [Sarnthein *et al.*, 2003a] SST reconstruction is marked by a greatly reduced sea-ice extent in the North Atlantic Ocean. Thus the GLAMAP winter sea-ice boundary is similar to the CLIMAP summer sea-ice boundary, and the Nordic Seas are even ice-free during summer [Sarnthein *et al.*, 2003b]. Furthermore, the GLAMAP SST is higher than in the CLIMAP reconstruction in the subtropical to polar North Atlantic Ocean, but lower in the tropical and South Atlantic Ocean. Finally, in the Atlantic sector of the Southern Ocean, there is more sea ice in the Drake Passage during winter, but less sea ice at the northern boundary of the Weddell Sea [Gersonne *et al.*, 2003].

[5] In conjunction with measurements of the oxygen isotopic composition of foraminiferal carbonate $\delta^{18}\text{O}_\text{c}$, the relatively high SST in the subpolar to polar North Atlantic Ocean yields a high sea-surface salinity and thus implies a high sea-surface density, which suggests that a very dense

Table 1. GLAMAP Data Employed for This Study

Region, Season ^a	Organisms ^b		Method ^c	Age, ^d ka BP	Reference
Tropical to North Atlantic, February/August	F		MAT	22–18	Pflaumann <i>et al.</i> [2003]
South to tropical Atlantic, annual mean/seasonality	F		TF	23–19	Niebler <i>et al.</i> [2003]
South Atlantic, February	F R D		TF MAT	23–19	Gersonde <i>et al.</i> [2003] Niebler and Gersonde [1998] Abelmann <i>et al.</i> [1999] Zielinski <i>et al.</i> [1998]
<i>SST</i>					
North Atlantic, February/August	via SST	22–18	Pflaumann <i>et al.</i> [2003]		
South Atlantic, August	D	A	23–19		Gersonde <i>et al.</i> [2003] ^e Gersonde and Zielinski [2000]
<i>Ice Cover</i>					

^aAugust indicates the three months July–September. Likewise, February denotes January–March. “Winter” and “summer” would have been more appropriate but could cause confusion when considering the Southern and Northern Hemispheres. To avoid this, we adhere to the months’ names.

^bAbbreviations are as follows: F, foraminifera; R, radiolaria; D, diatoms; C, coccolithophores; and Dc, dinocysts.

^cTF: Transfer functions. Abbreviations are as follows: MAT, modern analog technique and A, abundance.

^dCalendar ages.

^e“Average sea-ice” curve.

North Atlantic Deep Water (NADW) mass was formed at the LGM. Since the available proxy data indicate that below a depth of 2000 m the glacial Atlantic Ocean was filled with a cold, nutrient-rich and “old” water mass of southern origin, an even denser glacial Antarctic Bottom Water (AABW) mass had to be formed in the Southern Hemisphere [Zahn and Mix, 1991]. A possible mechanism to produce such a water mass could have been an intensified winter sea-ice formation in the southern Weddell Sea with its associated salt rejection and brine release [Mackensen *et al.*, 1996].

[6] The glacial ocean has been studied with a number of ocean general circulation models (OGCMs) using air temperature and freshwater flux from an atmospheric model [Lautenschlager and Herterich, 1990; Bigg *et al.*, 1998], reconstructions of SST and SSS [Seidov *et al.*, 1996; Winguth *et al.*, 1999], an energy balance model for the temperature boundary condition [Fieg and Gerdes, 2001] or a combination of global and regional modeling [Schäfer-Neth and Paul, 2001]. Two coupled model studies were carried out with intermediate complexity models [Ganopolski *et al.*, 1998; Weaver *et al.*, 1998]. Hewitt *et al.* [2001] presented the first multicentury simulation with a three-dimensional atmosphere-ocean general circulation model. Further coupled model experiments were performed by Kitoh *et al.* [2001] and Shin *et al.* [2003].

[7] Most of the model studies have focused on the deep-ocean circulation. Some have obtained a meridional overturning circulation weaker, others stronger than today. Hence on the model side so far no definite answer has been given to the question whether the formation of NADW at the LGM was weakened or not. On the data side, Yu *et al.* [1996] deduced a NADW export similar to today, but the re-evaluation of their Pa/Th data by Marchal *et al.* [2000] pointed to a reduction. The available $\delta^{13}\text{C}$ data is also sometimes interpreted as a weakening and shoaling of NADW [e.g., Duplessy *et al.*, 1988; Sarnthein *et al.*, 1994].

[8] In our present work, we used an OGCM with high vertical resolution, low vertical diffusion and isopycnal

mixing and imposed restoring boundary conditions on temperature and salinity. We carried out a sensitivity experiment with the GLAMAP SST reconstruction and no glacial SSS anomaly other than the global offset. To test whether intensified winter sea-ice formation in the southern Weddell Sea is indeed a credible mechanism to produce a cold and dense AABW, we performed three glacial experiments subject to glacial SSS distributions that differed in the size of the salinity anomaly applied to the Weddell Sea.

[9] We show that the stratification of the sub-surface glacial ocean can be related to the sea-surface density reconstructed from the paleo-SST and -SSS distributions. In the analysis of our experiments, we focused on the properties of the thermocline, which plays an important role in the cycling and vertical distribution of nutrients and carbon. The glacial thermocline turned out to be colder, shallower and better ventilated than today [cf. Slowey and Curry, 1995], whereas the meridional overturning circulation was similar. In the experiment with the largest salinity anomaly applied to the Weddell Sea, a very cold and salty water mass was formed that filled the Atlantic Ocean from the bottom up to a depth of 2000 m [cf. Mackensen *et al.*, 2001; Adkins *et al.*, 2002].

2. Methods

2.1. Model Forcing Fields: SST, SSS, and Wind Stress

2.1.1. SST and Ice Cover

[10] The SST reconstructions were carried out using different methods and were based on different proxy data. Although the definition of the LGM time slice was nearly the same, it was not identical in all cases, and the regions studied varied between the institutes involved in the GLAMAP project (Tables 1 and 2; Figure 1, top row). Therefore we had to carefully check the data prior to their interpolation in order to minimize artificial gradients between the study areas, and to avoid contradictions where the same area was sampled by different groups. Some regions were still void of data. Since this would have caused the interpolation to go astray, we extrapolated the isolines by

Table 2. Supplemental Data Collected for This Study

Region, Season ^a	Organisms ^b	Method ^c	Age, ^d ka BP	Reference
North Atlantic, August	Dc	MAT	23–19	<i>De Vernal et al. [2000]</i>
Atlantic, February/August	F	MAT	18^{14}C	<i>Prell [1985]</i>
Mediterranean, February/August	F	TF	18^{14}C	<i>Bigg [1994]</i>
Global Ocean, February/August	F R D C	TF	18^{14}C	<i>CLIMAP Project Members [1981]</i>
			<i>SST</i>	
North Atlantic, February/August	Dc	MAT	23–19	<i>De Vernal et al., 2000</i>
Global Ocean, February/August	via SST	18^{14}C		<i>CLIMAP Project Members [1981]</i>
			<i>Ice Cover</i>	
South Atlantic ^e				
North Atlantic ^f				
			<i>Planktic Foraminiferal $\delta^{18}\text{O}$</i>	

^aAugust indicates the three months July–September. Likewise, February denotes January–March. “Winter” and “summer” would have been more appropriate but could cause confusion when considering the Southern and Northern Hemispheres. To avoid this, we adhere to the months’ names.

^bAbbreviations are as follows: F, foraminifera; R, radiolaria; D, diatoms; C, coccolithophores; and Dc, dinocysts.

^cTF: Transfer functions. Abbreviations are as follows: MAT, modern analog technique and A, abundance.

^dCalendar ages, if not marked as ^{14}C .

^eReferences for South Atlantic are: *Melles [1991]* and *Duplessy et al. [1996]*.

^fReferences for North Atlantic are: *Kellogg et al. [1978]*, *Ruddiman and McIntyre [1981]*, *Jansen and Erlenkeuser [1985]*, *Zahn et al. [1985]*, *Bard et al. [1987]*, *Morris [1988]*, *Jones and Keigwin [1989]*, *Keigwin and Boyle [1989]*, *Jansen and Veum [1990]*, *Vogelsang [1990]*, *Duplessy et al. [1991]*, *Lackschewitz [1991]*, *Veum et al. [1992]*, *Duplessy et al. [1992]*, *Köhler [1991]*, *Jünger [1993]*, *Weinelt [1993]*, *Sarnthein et al. [1995]*, and *Weinelt et al. [1996]*.

Pflaumann et al. [2003] into the western Atlantic Ocean to connect them with the data that were available in this part of the basin.

2.1.1.1. Selection of Source Data

[11] Our gridded Atlantic-wide SST fields are based on the following three GLAMAP data sets:

[12] 1. Set 1 [*Pflaumann et al., 2003*]. By subjective interpolation of an extensive set of core-based SST reconstructions from assemblages of fossil planktonic foraminifera, *Pflaumann et al. [2003]* constructed SST maps that cover almost the entire Atlantic Ocean. At the cold end of the temperature range, the SIMMAX method [*Pflaumann et al., 1996*] tends to yield too high SSTs [*Weinelt et al., 2001*]. However, according to modern SSTs “reconstructed” from core-top faunal assemblages, sea-ice edges were located at the 3°C and 0.4°C isotherms in boreal summer and winter, respectively [*Sarnthein et al., 2003b*]. In our numerical model, the ice cover was imposed as part of the surface boundary condition on temperature. Therefore we set the SSTs to -1.5°C at and to -1.8°C just poleward of these isotherms. This lead to an “ice nose” extending westward off Ireland, which was caused by low SSTs at a number of sediment core sites. We interpret this feature as an occasional ice surge originating from the eastern part of the Norwegian Sea, but not as a persistent feature of the glacial climate.

[13] 2. Set 2 [*Niebler et al., 2003*]. From the annual mean SSTs and their seasonalities reconstructed by *Niebler et al. [2003]* for the South Atlantic Ocean, we computed the maximum and minimum glacial temperatures and attributed the maximum in general to February (that is, austral summer) and the minimum to August (that is, austral winter). However, in the equatorial ocean, this assignment may not necessarily be correct. In fact, a smooth connection of the South Atlantic data to the North Atlantic values was only possible by reversing the attribution for the seven

northernmost cores. This is similar to modern SSTs, for which the “thermal equator” lies at about 5° to 10°N , closely tied to the Intertropical Convergence Zone. Although the data by *Niebler et al. [2003]* have not directly been included in our gridding process, they were taken into account by *Pflaumann et al. [2003]* in the construction of the isotherms of their SST maps.

[14] 3. Set 3 [*Gersonde et al., 2003*]. For the Atlantic sector of the Southern Ocean, an extensive set of SST estimates was provided by *Gersonde et al. [2003]*, based on faunal assemblages of foraminifera [*Niebler and Gersonde, 1998*], radiolaria [*Abelmann et al., 1999*], and diatoms [*Zielinski et al., 1998*]. *Gersonde et al.* also reconstructed the seasonal sea-ice cover for Antarctica. According to R. *Gersonde* (personal communication, 2002), the ice edges must be considered more reliable than the SST reconstructions and we discarded all SST estimates poleward of them.

[15] To fill in the remaining gaps, especially in the western Atlantic Ocean and its marginal seas, we included other data as follows:

[16] 4. Set 4 [*De Vernal et al., 2000*]. *De Vernal et al. [2000]* estimated August and February SSTs all over the subpolar and polar North Atlantic Ocean based on dinoflagellate cysts, in part overlapping the SIMMAX data by *Pflaumann et al. [2003]*. However, we used only the western part between Newfoundland and Greenland for August. The northeast and February temperatures of this reconstruction are much higher than the SIMMAX SSTs, some even higher than modern SSTs. As pointed out by *De Vernal et al. [2002]*, these high SSTs could reflect a very fresh and therefore very thin surface layer that might have warmed rapidly during glacial summer. Such a layer would have had only a minor dynamical effect, given the density increase during winter ice formation. We therefore decided to discard these data in favor of the SIMMAX set.

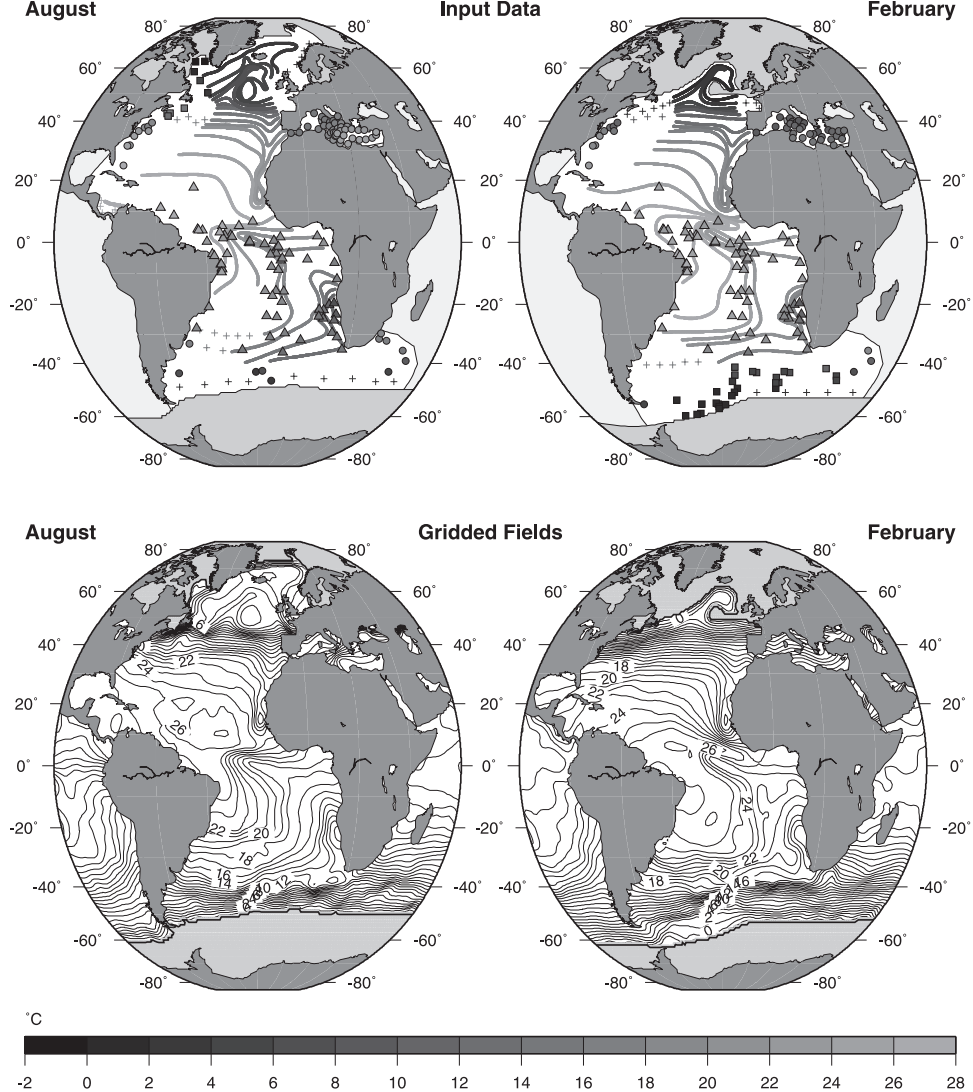


Figure 1. Glacial sea surface temperature (°C). (top) Database. Isolines, Pflaumann *et al.* [2003]. Triangles, Niebler *et al.* [2003]. Squares, De Vernal *et al.* [2000] (August) and Gersonde *et al.* [2003] (February). Circles, Prell [1985] (Atlantic) and Bigg [1994] (Mediterranean). Blue (medium gray), ice cover after Pflaumann *et al.* [2003], De Vernal *et al.* [2000], and Gersonde and Zielinski [2000]. Light gray, SST data taken from CLIMAP Project Members [1981]. Pluses, artificial tie points to prevent unrealistic gradients in the interpolated fields. (bottom) Resulting 1° × 1° gridded fields; white lines denote ice edge. See color version of this figure at back of this issue.

[17] 5. Set 5 [Prell, 1985]. The data introduced so far do not extend to the western parts of the Atlantic Ocean. Here and to the east of South Africa, we used the revised CLIMAP SSTs by Prell [1985].

[18] 6. Set 6 [Bigg, 1994]. Glacial SSTs for the Mediterranean were sampled from the maps by Bigg [1994] at a spatial resolution of 2–5 degrees.

[19] 7. Set 7 [CLIMAP Project Members, 1981]. Except for a small region in the Gulf of Mexico, no CLIMAP data were included in our compilation for the Atlantic Ocean, but to force our global ocean model, we used the CLIMAP reconstruction for the Indian and Pacific Oceans and the corresponding sectors of the Southern Ocean.

[20] 8. Ice Edges. In the Northern Hemisphere, we extended the SST-based seasonal ice cover reconstruction of Pflaumann *et al.* [2003] to the west according to the February and August ice estimates of De Vernal *et al.* [2000]. For the Southern Ocean, we used the average sea-ice estimate during austral winter by Gersonde *et al.* [2003] and Gersonde and Zielinski [2000]. However, there is only a crude estimate available for austral summer, being somewhere between the modern summer conditions in the western, but close to modern winter conditions in the eastern South Atlantic Ocean [Gersonde *et al.*, 2003]. We therefore chose a line starting at 64°S in the Drake Passage and reaching 62°S south of Africa. Both seasonal ice lines

for the South Atlantic Ocean were smoothly joined to the CLIMAP ice edges in the Pacific and Indian Oceans.

2.1.1.2. Gridding and Seasonal Cycle

[21] The compiled data set is characterized by a number of features to be kept in mind when choosing an interpolation scheme. First, the North Atlantic isoline data already represent an interpolation based on an (admittedly subjective) interpretation of the paleoceanographic data. One of the aims of our study was to test this interpretation with a circulation model, and the information conveyed by the isolines should not have been lost in the gridding process. Second, the Atlantic Ocean is quite densely sampled in some areas, but very sparsely in others, necessitating an algorithm that accounts for the small-scale information but equally well can fill up these blank spaces. For these reasons we chose the method of variogram analysis and kriging, carried out with the gamv2 and okb2d routines of the GSLIB package [Deutsch and Journel, 1992]. Because the data set spans the whole Atlantic Ocean on a spherical grid, we rewrote these routines to use spherical instead of cartesian coordinates [Schäfer-Neth *et al.*, 1998].

[22] Even at first glance, the data show different spatial variabilities, depending mainly on latitude. To account for this, we divided each of the monthly sets into 10 latitude belts, each 30 degrees wide and overlapping the next by 15 degrees. That is, the first contained all points between 75°S and 45°S, the second from 60°S to 30°S, and so on. For each of these belts, five experimental variograms were computed, one omnidirectional and four in the S-N, W-E, SW-NE and SE-NW directions, the latter four with an angular tolerance of 45 degrees. Lag spacing was set to a maximum of 50 lags of 2 degrees. The variogram models were fitted to the pair of perpendicular variograms showing maximum and minimum variance. In some cases, especially in the high latitudes with very little overall variance, the omnidirectional variograms were used for fitting. Given the variogram models, the data were kriged for each belt to a regular $1^\circ \times 1^\circ$ grid. After this, the belts were joined by weighted averaging, such that the weight increased linearly from zero at a belt's southern limit to one at its center and dropped again to zero at its northern limit. The resulting Atlantic fields (Figure 1, bottom row) were merged with the global *CLIMAP Project Members* [1981] data sets for February and August, with an additional 2° moving average over the whole combined data set.

[23] Directly fitting a sinusoid through the reconstructed February and August SSTs led to glacial SSTs overshooting the modern ones by several degrees in the North Pacific Ocean. Therefore we adopted the *Paleoclimate Modelling Intercomparison Project (PMIP)* [1993] procedure of first fitting a seasonal cycle to the glacial-to-modern anomalies (Figure 2) and then adding them to the modern monthly SSTs. Modern temperatures were taken from the 10 m *World Ocean Atlas (WOA)* [1998] data, corresponding to the 10 m temperatures against which the various methods for reconstructing SSTs employed in the GLAMAP project were calibrated.

[24] Although the gridding described above yields closed ice covers for February and August, the method for reconstructing the seasonal cycle does not because it averages temperature at a given location, but not the position of the

ice edge. In fact, it would produce an SST cycle between freezing and summer temperature within the area of seasonal ice retreat and advance, but no retreating or advancing ice edge. Therefore we constructed five additional monthly ice cover fields for the Northern Hemisphere, with an ice edge varying between the minimum and maximum extent that were superimposed on the monthly SST fields. In the Southern Hemisphere, the latitude of the ice edge was linearly interpolated in time between summer and winter.

2.1.2. $\delta^{18}\text{O}_c$ and SSS

[25] Sea surface salinity was computed using the approach of Schäfer-Neth [1998] and Schäfer-Neth and Paul [2001] from the temperatures presented in the previous section and a collection of 143 deep sea sediment cores from the North Atlantic Ocean for which $\delta^{18}\text{O}_c$ measurements from fossil foraminifer shells are available (Table 2). This approach requires a correlation between the isotopic composition of seawater $\delta^{18}\text{O}_w$ and salinity that varies with local influences like seasonal sea-ice coverage, runoff from glaciers and riverine inputs.

2.1.2.1. SSS at the Sediment Core Locations

[26] In a similar manner to Paul *et al.* [1999], we computed a $\delta^{18}\text{O}_w$ -SSS relation varying with latitude from the Atlantic GEOSECS data [Östlund *et al.*, 1987] taken from the GISS $\delta^{18}\text{O}$ Database [Bigg and Rohling, 2000; Schmidt *et al.*, 1999]. The $\delta^{18}\text{O}_w$ -to-SSS slope varies between 1.85 at 45°N and 1.6 at 75°N. The computation of the fit coefficients was carried out using only the GEOSECS data, because the complete data set includes a large number of very low $\delta^{18}\text{O}_w$ and salinity values from the Labrador Sea that are not representative for most of the North Atlantic Ocean and would have considerably biased the result. We attempted to derive a seasonal $\delta^{18}\text{O}_w$ -salinity relation to resolve the influence of sea-ice melt and formation. For the tropical and subtropical latitudes, the relations for boreal summer and winter turned out to be quite similar to the annual one. The same was true for the summer and the annual relations in higher latitudes, but the database was too sparse to support a reliable relation for high-latitude boreal winter. However, according to Schmidt [1999], the effect of an incorrect $\delta^{18}\text{O}_w$ -SSS relation is comparatively low when salinities are high, which is surely the case for the present study. In addition, the measured glacial $\delta^{18}\text{O}_c$ values are believed to pertain to the warm season which is well documented in the GEOSECS data. Therefore we employed the annual relation.

[27] After sampling the interpolated August SST field at the core sites and correcting SST to the calcification temperature of the respective foraminifer species according to the relations summarized in Schäfer-Neth [1998], we computed $\delta^{18}\text{O}_w$ from $\delta^{18}\text{O}_c$ and SST using the paleotemperature equation of Epstein *et al.* [1953]. By applying the regressions derived from the GEOSECS data and the global $\delta^{18}\text{O}_w$ and SSS changes of 1.2% and 1.07, we arrived at LGM August SSS estimates for the core locations.

2.1.2.2. Gridding and Seasonal Cycle

[28] The SSS gridding process was carried out in the same manner as outlined in the section on SST. However, directly gridding the SSS estimates from the core locations did not yield a field that could be seamlessly incorporated into any global data set. Instead we computed the glacial-to-modern

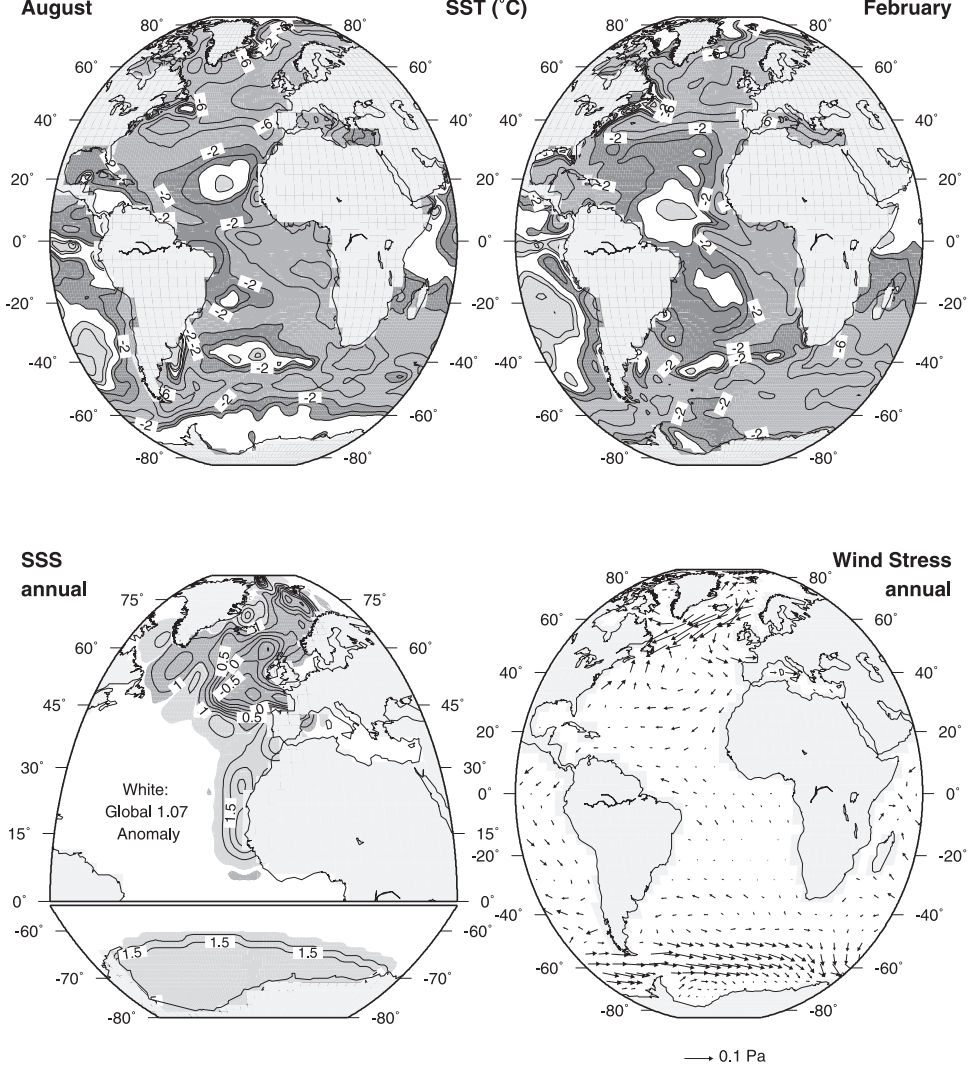


Figure 2. Glacial minus modern anomalies of the model forcing data. Step-like structures along the coasts indicate the model's spatial resolution. (top) SST (contours at ± 0.5 , ± 1 , ± 2 , ± 4 , ± 6 , and $\pm 10^{\circ}\text{C}$). (bottom) SSS (dark shading, below global anomaly; light shading above, contour interval is 0.25) and wind stress (Pa).

SSS anomalies, using the summer *WOA* [1998] 10 m data for reference. This set of anomalies was supplemented by points set to the global anomaly of 1.07 in regions where no $\delta^{18}\text{O}_\text{c}$ cores were available and then kriged onto the regular $1^{\circ} \times 1^{\circ}$ grid (Figure 2, lower left). The combination of a $\delta^{18}\text{O}_\text{w}$ salinity relation varying smoothly with latitude and the interpolation of anomalies avoids the difficulties faced by *Seidov et al.* [1996] and *Seidov and Haupt* [1997]: They used a fixed relation for two (much sparser) $\delta^{18}\text{O}_\text{c}$ data sets, one between 40°N and 50°N , the other north of 50°N , which led to artificial offsets between and especially south of these regions.

[29] There is evidence for an additional glacial SSS anomaly in the Weddell Sea [Melles, 1991; Duplessy *et al.*, 1996]. To elucidate its effect on the glacial Atlantic Ocean, we constructed two additional anomaly fields with local SSS enhancements by 0.55 (as shown in Figure 2) and 1 off the Antarctic coast.

[30] The seasonal SSS cycle was constructed as in *Schäfer-Neth and Paul* [2001] by adding the gridded anomaly field for boreal summer to the modern monthly salinity data, these as well taken from the 10 m *WOA* [1998] analyses.

2.1.3. SST and SSS Uncertainties

[31] The uncertainty of the SST estimates at individual core sites is typically in the order of 1°C , regardless of the reconstruction method chosen. Specifically for the SIMMAX method, there is a tendency of overestimation at the cold end that might amount to more than 1°C [*Weinelt et al.*, 2001]. We overcame this problem by including additional information on the position of the ice edges and setting the SSTs to the freezing point over the appropriate areas.

[32] The uncertainty of the reconstructed SSS is determined by a couple of parameters. First, there are the measurement errors that enter the paleotemperature equation: an SST uncertainty around 1°C and a $\delta^{18}\text{O}_\text{c}$ error of typically 0.1. Error propagation yields a $\delta^{18}\text{O}_\text{w}$ error of about

0.4 and, taking into account the relation between $\delta^{18}\text{O}_w$ and salinity, an SSS error of about 0.7. This is about one quarter of the zonal and meridional differences within the reconstructed SSS anomalies in the subtropical and subpolar North Atlantic Ocean (Figure 2, bottom left). Thus the overall anomaly pattern would not change very much owing to false SST or incorrect $\delta^{18}\text{O}_c$ data. This is especially the case given the high spatial sampling density with more than 140 cores contained in the area for which we reconstructed SSS. Unfortunately, the absolute SSS value is a much less robust estimate than the local SSS gradients because it is affected by all of the parameters of the empirical relationships between SST, $\delta^{18}\text{O}_c$, $\delta^{18}\text{O}_w$ and SSS. Here the paleotemperature equation is the most critical. Representing a link between water temperature, water oxygen-isotopic composition and the isotope ratio fixed in the carbonate shells of the foraminifera, it is intimately tied to the life cycle of these organisms and varies depending on numerous parameters like the water masses in which the foraminifera grow, the season of reproduction, and the water depth preferred by the different biota. Even a single species may record different $\delta^{18}\text{O}_c$ values depending on when and where it is sampled. For example, *Simstich* [1999] and *Mulitza et al.* [2003] report a systematic contrast of 1 between shells of *Neogloboquadrina pachyderma* (sinistral) that were taken near the ocean surface and those recovered from core-top sediments, which are heavier owing to secondary calcification. Other species like *Globigerina bulloides* do not show such an offset. The adjustments we employed between SST and calcification temperature are essentially an attempt to compensate for these different offsets. If other species were included, SST adjustments of up to 4–5°C might be necessary, depending on the species, to yield a consistent $\delta^{18}\text{O}_w$ set [Bemis et al., 1998]. In his detailed summary of the errors caused by these vital effects, *Schmidt* [1999] estimates a total salinity error that may easily exceed 1 and reach even values around 1.8 in the tropics.

[33] We are aware that we have to take our SSS reconstructions with caution. However, we employ a large and extensive set of SST reconstructions and $\delta^{18}\text{O}_w$ data for a time slice that was defined in the same way for all contributing research groups. Thus any extraordinary error at a specific core location would immediately show up as an outlier in the gridded SST or SSS fields. In fact, we discarded one single $\delta^{18}\text{O}_c$ value from the subpolar North Atlantic Ocean based on such a judgment, and we regard our reconstruction as internally consistent, although possibly biased by a yet unknown global offset.

2.1.4. Wind Field

[34] The wind stress anomaly (Figure 2, lower right; Figure 3) for our glacial model experiments was derived from the control run of the European Centre/Hamburg atmospheric general circulation model (ECHAM3) at T42 resolution and a run that employed our GLAMAP SST compilation as bottom boundary condition (S. Lorenz and G. Lohmann, personal communication, 2001), but otherwise was set up according to the PMIP [1993] guidelines. The control run and a run based on the CLIMAP SST reconstruction are described by *Lorenz et al.* [1996].

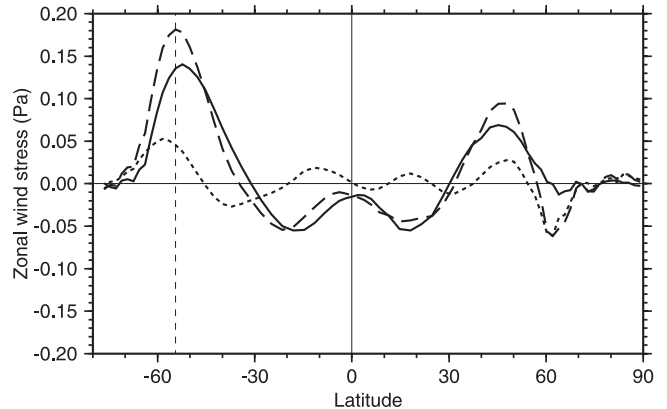


Figure 3. Glacial minus modern anomalies of the model forcing data. Annual and zonal mean of the zonal wind stress as simulated by the ECHAM3 atmospheric general circulation model. Solid line denotes control run. Dashed line denotes LGM run based on GLAMAP SST. Dotted line denotes anomaly. The dashed vertical line denotes the latitude of Cape Horn in the ocean model.

2.1.5. Availability

[35] The gridded $1^\circ \times 1^\circ$ SST and SSS reconstructions are available from the World Data Center for Paleoclimatology.¹

2.2. Model

[36] We used the Modular Ocean Model (MOM 2) of the Geophysical Fluid Dynamics Laboratory (GFDL) [*Pacanowski*, 1996]. The model domain was global. Its resolution, geometry and bottom topography were similar to the coarse-resolution model of *Large et al.* [1997]. The longitudinal resolution was constant at 3.6° , whereas the meridional resolution was 1.8° near the equator, decreased to a minimum of 3.4° away from the equator, then increased in midlatitudes as the cosine of latitude and was finally kept constant at 1.8° poleward of 60° . There were 27 vertical levels with monotonically increasing thickness from 12 m near the surface to 450 m near the bottom. The minimum model depth was 49 m, corresponding to 3 vertical levels. The maximum model depth was 5900 m.

[37] The modern bottom topography of the model was derived from the ETOPO5 topography data [*NCAR Data Support Section*, 1986]. To obtain the glacial bottom topography, we computed the glacial anomaly from the *Peltier* [1994] reconstruction and added it to the modern bottom topography. In both cases, after interpolating the topography to the model grid, we smoothed and adjusted it according to the procedure outlined by *Large et al.* [1997].

[38] The vertical diffusion coefficient was depth-dependent [*Bryan and Lewis*, 1979]:

$$A_{tv} = A_0 + \frac{C_r}{\pi} \arctan[\lambda(z - z_0)] \quad (1)$$

¹ Supporting data are available electronically at World Data Center-A for Paleoclimatology, NOAA/NGDC, 325 Broadway, Boulder, CO 80303 (e-mail: paleo@noaa.gov; URL: <http://www.ngdc.noaa.gov/paleo>).

where $A_0 = 0.7 \times 10^{-4} \text{ m}^2 \text{ s}^{-1}$, $C_r = 1.25 \times 10^{-4} \text{ m}^2 \text{ s}^{-1}$, $\lambda = 4.5 \times 10^{-4} \text{ m}^{-1}$ and $z_0 = 2500 \text{ m}$. Thus A_{tv} ranged from $0.1 \times 10^{-4} \text{ m}^2 \text{ s}^{-1}$ near the surface to $1.3 \times 10^{-4} \text{ m}^2 \text{ s}^{-1}$ near the bottom. Above the turnover depth z_0 , the vertical diffusion coefficient was smaller than in the previous studies by *Paul et al.* [1999] and *Schäfer-Neth and Paul* [2001]. According to the few available observational estimates, a low value of $0.1 \times 10^{-4} \text{ m}^2 \text{ s}^{-1}$ indeed seems to be appropriate below the thermocline and away from topography [*Ledwell et al.*, 1993].

[39] Another difference from the two previous studies was the use of isopycnal mixing and the mesoscale eddy tracer transport parameterization of *Gent and McWilliams* [1990]. The isopycnal diffusion and thickness diffusion coefficients were chosen to be equal, $A_1 = A_{ITD} = 0.5 \times 10^3 \text{ m}^2 \text{ s}^{-1}$, and the horizontal diffusion coefficient A_{hv} was set to zero. The vertical and horizontal viscosity coefficients were $A_{mv} = 16.7 \times 10^{-4} \text{ m}^2 \text{ s}^{-1}$ and $A_{mh} = 2.5 \times 10^5 \text{ m}^2 \text{ s}^{-1}$. Taken together, the low value of the vertical diffusion coefficient in the upper 2000 m and the isopycnal mixing parameterization allowed for a better representation of the upper ocean hydrology and circulation.

[40] For the momentum and barotropic integrations, the time step was 1800 s. The tracer time step was 2.5 days at all levels. All experiments were integrated for at least 2000 tracer years (Experiment M for 5000, Experiment G3 for 3700 tracer years). Fourier filtering was applied to the flow variables south of 71.1°S and north of 71.1°N , and to the tracer variables south of 70.2°S and north of 70.2°N .

[41] The surface momentum flux was given by the zonal and meridional wind stress components, and the net surface heat and freshwater fluxes were computed by restoring the potential temperature and salinity at the first model level to prescribed monthly SST and SSS with a relaxation timescale of 50 days relative to the upper 50 m.

2.3. Experimental Setup

[42] We carried out five model experiments, one for the modern and four for the LGM time slice:

[43] 1. Experiment M was subject to modern sea surface boundary conditions. The sea-surface temperature and salinity fields were taken from the 1998 World Ocean Atlas data for 10 m depth. The wind stress fields were derived from the NCEP reanalysis data covering the four years 1985 through 1988 [*Kalnay et al.*, 1996] as described by *Large et al.* [1997].

[44] 2. Experiment G0 employed the glacial SST reconstruction discussed in section 2.1.1 and the glacial wind stress anomaly described in section 2.1.4, added to the wind stress field of Experiment M. The SSS field was the same as in Experiment M except for global offset of 1.07.

[45] 3. Experiment G1 used in addition the glacial SSS field discussed in section 2.1.2.

[46] 4. Experiment G2 was run under the same conditions as Experiment G1, but with the 0.55 salinity anomaly in the Weddell Sea.

[47] 5. Experiment G3 employed the 1.0 salinity anomaly in the Weddell Sea.

[48] The difference between Experiment M and Experiment G0 isolates the SST effect on the circulation, while

Experiment G0 combined with Experiment G1 highlights the effect of North Atlantic salinity changes.

3. Results

3.1. Density

[49] The mixed layer density (expressed as the deviation from 1000 kg m^{-3}) in Experiment M is characterized by values higher than 27 kg m^{-3} in the high latitudes of either hemisphere (Figure 4). In the glacial experiments, the global mean SST is lower by about 1.2°C and the global mean SSS is higher by about 1. Correspondingly, the mixed layer density exhibits a general increase by about 1 kg m^{-3} , as well as a local enhancement in the coastal upwelling areas near the eastern boundary. As compared to the modern case, the isopycnals are first oriented more zonally near the western boundary and then deflected equatorward. Experiment G0 with no glacial SSS anomaly other than the global offset shows values beyond 29 kg m^{-3} in the northeastern North Atlantic Ocean. These high values are absent from Experiments G1–G3 because of the low salinity anomaly reconstructed for this region.

[50] In Experiment G3, the Atlantic sector of the glacial Southern Ocean is characterized by a region of high sea-surface density, which extends to the northern rim of the Weddell Sea and into the zone of assumed increased winter sea-ice coverage and is due to the additional salinity anomaly. In Experiment G2, the Weddell Sea surface density is less dominant and only slightly higher than the surface density of the North Atlantic Ocean (Figure 5, top), comparable to the modern situation. In Experiment G1, and even more so in Experiment G0 owing to the large values in the northeastern North Atlantic Ocean, the density contrast between the high northern and southern latitudes is reversed. Experiment M exhibits three pronounced sea-surface density gradients in the North Atlantic Ocean: in the subtropical, subpolar and polar regions (Figure 5, top, solid horizontal bars). The glacial experiments show no polar gradient, but only the subtropical and subpolar gradients, with the subpolar one being stronger than in Experiment M (Figure 5, top, dashed horizontal bars).

[51] The sea surface buoyancy flux (Figure 6) diagnosed from the restoring boundary conditions on Experiment M clearly reflects the oceanic heat loss to the atmosphere along the paths of the Gulf Stream, the North Atlantic Drift, and the Brazil Current. In the high latitudes of the winter hemisphere, negative values correspond to the formation of deep and bottom waters. In Experiment G3, positive values along the northern rim of the Weddell Sea and west of Ireland indicate freshening, presumably owing to an increased influence of melting sea ice.

[52] The rate of sea-ice formation and melting in the inner Weddell Sea can be inferred from the restoring boundary condition on salinity [*Toggweiler and Samuels*, 1995a]. For Experiment M, the implied net freezing rate is 0.061 m a^{-1} and the divergence of the net surface freshwater flux is 4.87 mSv ($1 \text{ mSv} = 10^{-3} \text{ Sv}$, Table 3). These values change sign in Experiments G0–G2. In Experiment G3, the fluxes are of the same sign as in Experiment M, but considerably larger.

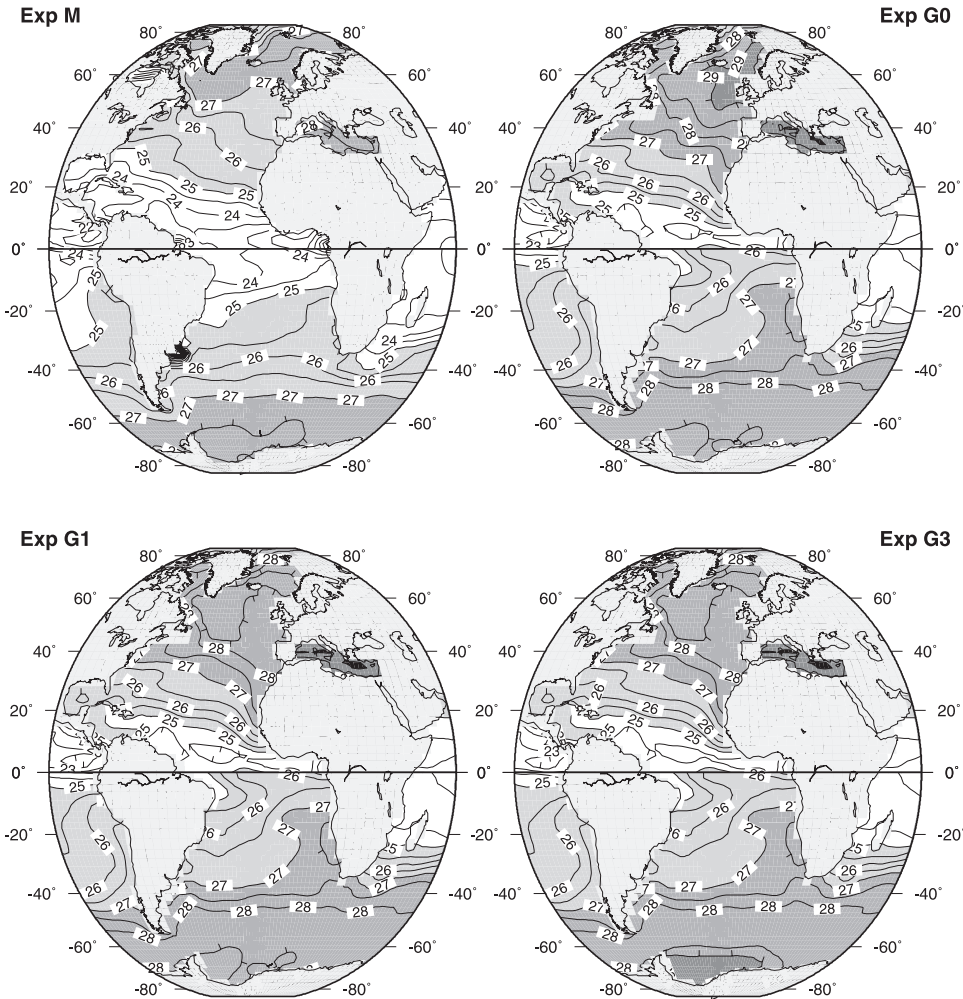


Figure 4. Modeled mixed layer density in the winter hemisphere (during March and September, respectively). The contour interval is 0.5 kg m^{-3} .

[53] Our model develops maximum mixed layer depths in the high latitudes during winter, shortly after the highest surface densities have been reached (Figure 7). In Experiments G1–G3 as opposed to Experiment M, very deep convection occurs south of Iceland between 30° and 40°W , where the high-salinity tongue is reconstructed. East of this convection site, the low sea-surface salinity yields a mixed layer much shallower than at present. North of Iceland, we find ongoing deep convection in the Nordic Seas at the LGM. Convection in the northeastern Weddell Sea is strongly increased in Experiment G3 owing to the high additional salinity anomaly.

3.2. Thermocline Ventilation

[54] The ventilation of the thermocline is not obvious from the distribution of mixed layer depth, although the 200-m isoline extending from the northeast North Atlantic Ocean to the southwest is a first indication (Figure 7). To find out where exactly water is subducted from the mixed layer into the thermocline, we followed the prescription of Sprintall and Tomczak [1992] and Tomczak and Godfrey [1994]. First we obtained the thickness of the surface isothermal layer

from the model output by extracting the depth where the temperature differs from the temperature at the surface by more than 0.5°C . Then we determined the thickness of the surface isopycnal layer by computing the depth where the density is larger than the density at the surface by an amount which corresponds to the temperature change of 0.5°C used in the construction of the surface isothermal layer. The depth difference between the surface isothermal and isopycnal layers (termed barrier-layer thickness) can be different from zero (Figure 8). Negative differences in the subtropics reliably indicate the subduction of thermocline water [Tomczak and Godfrey, 1994].

[55] In the South Atlantic Ocean, the maximum negative difference is found in the Argentine Basin, between 40°S and 45°S in Experiment M and a little further to the north in Experiments G0–G3. Thus the thermocline is ventilated at the Subtropical Front. The situation in the North Atlantic Ocean is more complex. In Experiment M, there is a single maximum negative difference in the Bay of Biscay. Experiment G0 is similar, but displays a secondary maximum negative difference between 30° and 40°W . In the other glacial experiments, the reconstructed low salinity in the

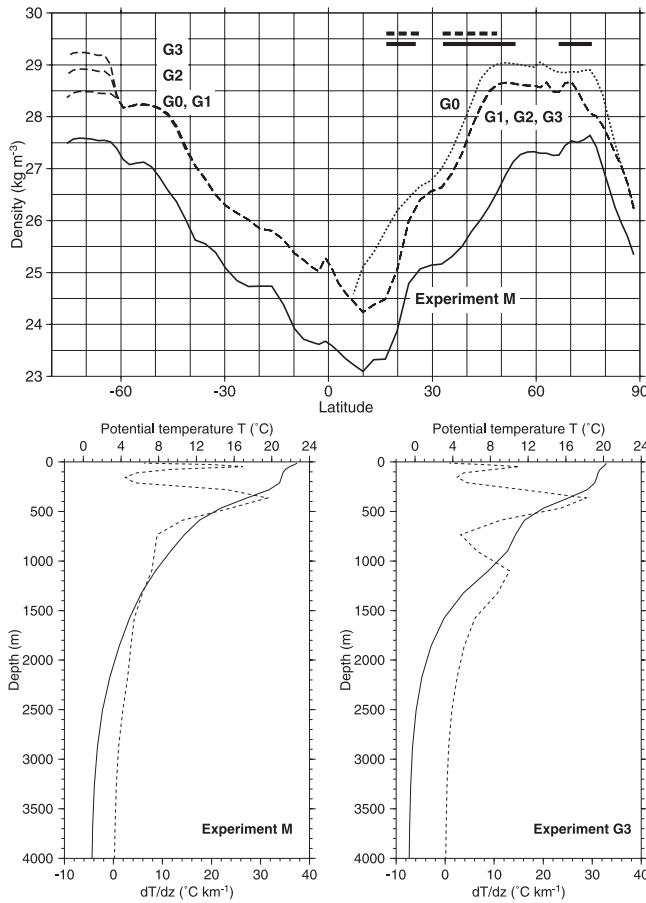


Figure 5. (top) Annual mean sea surface density of the western Atlantic Ocean for all five experiments. Solid (Experiment M) and dashed (Experiments G0–G3) horizontal bars indicate the extent of the meridional temperature gradients associated with water mass formation in the Northern Hemisphere. Note that in G0 the steepest density gradients in high northern latitudes occur in the eastern part of the Atlantic Ocean and the meridional section was shifted accordingly. (bottom) Profiles of annual-mean temperature and vertical temperature gradient at 33°N from Experiments M (left) and G3 (right).

Bay of Biscay in combination with the reconstructed high-salinity tongue near 30° shifts the modern region of thermocline ventilation to the southwest. Furthermore an additional ventilation site appears south of Greenland that feeds into the intermediate water.

[56] From the thickness of the barrier layer and the distribution of the mixed layer density (cf. Figure 4), we derived the density criteria for tracing the base of the ventilated thermocline (Figure 9). To have a common definition for the whole Atlantic Ocean, we chose $\sigma_0 = 26.9 \text{ kg m}^{-3}$ for the control and $\sigma_0 = 28.2 \text{ kg m}^{-3}$ for all glacial experiments. In Experiment M, the ventilated thermocline is shallow near the equator (400–450 m) and at the poleward boundaries of the subtropical gyres. It deepens toward the gyre centers where it reaches up to 650 m. During the LGM (as shown for Experiment G3 in Figure 10), the

tropical thermocline between 20°S and 20°N is up to 50 m shallower than today. In the extra-tropics, the thermocline deepens in the gyre centers and near the southern Subtropical Front and shoals to the south of Cape of Good Hope. The thermocline depth in Experiment G0 shows a pattern similar to the other glacial experiments, but is about 50 m shallower, with the region of ventilation in the North Atlantic Ocean shifted still further to the southwest (not shown).

[57] The thermocline water cools by 2–3°C in the North Atlantic Ocean and 4–5°C in the South Atlantic Ocean (Figure 10). While the cooling in the North Atlantic Ocean is due to lower temperatures at the sea surface and enhanced ventilation, in the South Atlantic Ocean, less warm water is imported from the Indian Ocean and more and colder water is subducted at the Subtropical Front (Figure 11). In the seasonal thermocline (the lower boundary of which is defined as the annual maximum of mixed layer depth), there is a more zonal North Atlantic Current and a stronger recirculation in the northern subtropical and subpolar gyres. The water recirculating within the subtropical gyre is eventually entrained into the thermocline, in which the southwest transport gradually increases (Figure 11).

[58] Owing to the ice-free conditions in the glacial Norwegian Sea, there is still an active although somewhat reduced inflow into the Nordic Seas (below the depth of the seasonal thermocline, not shown). In the Southern Hemisphere at the LGM, less water is advected from the Indian into the South Atlantic Ocean, in the thermocline as well as in the mixed layer and at intermediate water depth. The Benguela Current turns out to be weaker than today, and the South Atlantic Current and the Antarctic Circumpolar Current are shifted southward by one grid row.

3.3. Atlantic Water Mass Characteristics

[59] The large-scale ocean circulation and the spreading of newly formed water masses is generally most intense at the western boundaries of the oceans. Therefore we chose a section along the western Atlantic Ocean as shown in Figure 7 to illustrate the modeled T and S distributions.

[60] The different sea-surface conditions in our experiments have a profound effect on the characteristics of the main water masses (Figure 12). In the T-S diagram for the western Atlantic Ocean of Experiment M, the warm and salty NADW and the cold and fresher Antarctic Bottom Water (AABW) form the main water masses and are connected by a mixing line. Referenced to a depth of 3000 m, the average density contrast between both water masses amounts to 0.4 kg m^{-3} .

[61] Using glacial SST and adding the global 1.07 salinity anomaly in Experiment G0 leads to a considerable rearrangement of the water masses in the T-S diagram: The high densities in the northeastern North Atlantic Ocean cause a northward shift of the convection sites in this region. Hence Arctic Bottom Water (ABW) is fed by colder water around 0°C (Figure 13). Likewise, the formation region of NADW is confined to a narrower latitude belt than in the control run (cf. Figure 14), which results in a smaller temperature range for NADW; at the same time, its salinity is increased. AABW is formed further to the north than today (cf. Figure 13) and

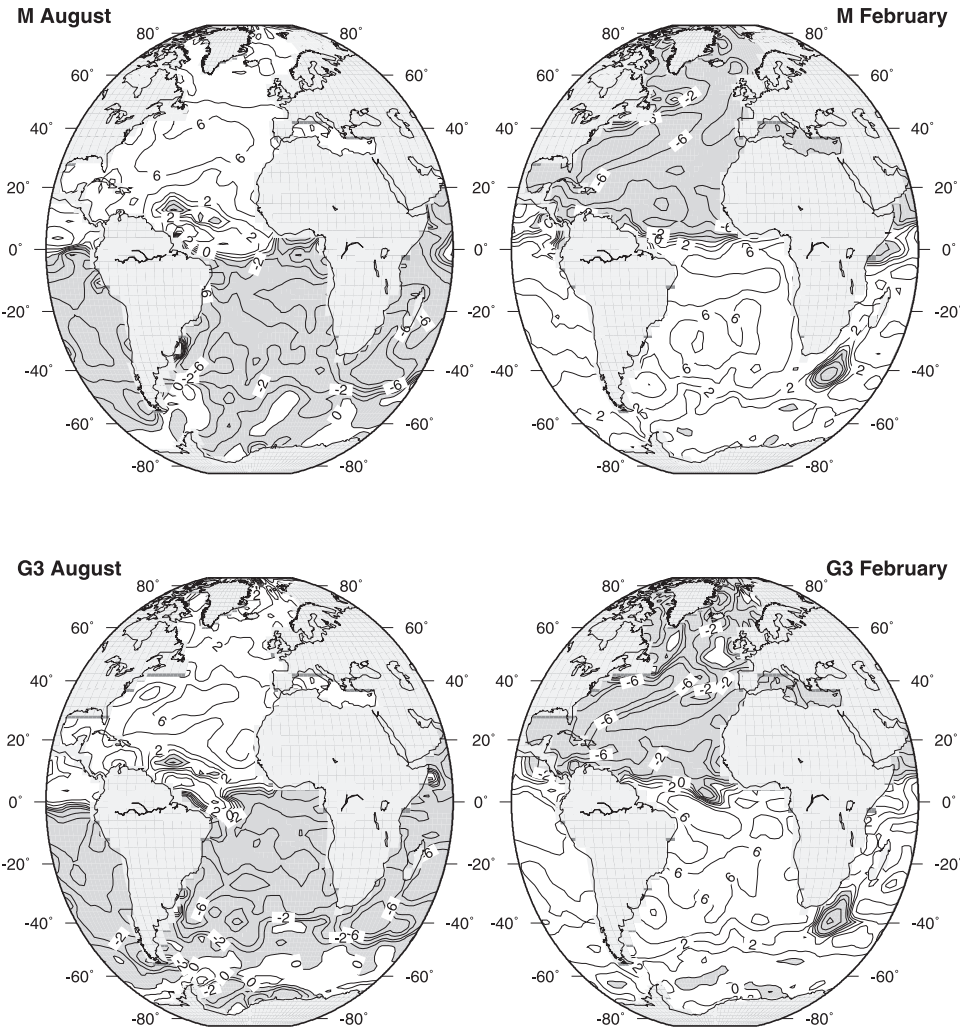


Figure 6. Sea-surface buoyancy flux as diagnosed from the restoring boundary conditions on SST and SSS. The contour interval is $2 \text{ kg m}^{-2} \text{ s}^{-1}$. Negative values (shaded) indicate an increase of sea-surface density. (top) Experiment M. (bottom) Experiment G3.

turns out to be much warmer albeit denser than in Experiment M.

[62] Switching to reconstructed glacial salinities in Experiment G1, NADW cools by about 0.5°C as compared to Experiment G0. In spite of that, its density is slightly decreased owing to the lower SSS in the formation region. In Experiment G1, AABW is as warm as in Experiment G0 but less salty, although the haline forcing field is identical over the Southern Ocean. Both model runs lack deep convection in the southern Weddell Sea, and the deep and bottom water salinity signature is overprinted by the admixture of salty water from the North Atlantic Ocean and a smaller amount of less salty water from the northern rim of the Weddell Sea. This yields small density contrasts between AABW and NADW (Figure 12): 0.15 kg m^{-3} in Experiment G0 and 0.3 kg m^{-3} in Experiment G1, cf. Figures 13 and 14. The salinity increase of AABW is more pronounced in Experiment G0 owing to its higher meridional overturning (cf. Figure 15) and the correspondingly more efficient advection of NADW that is even saltier than

in Experiment G1 owing to the generally higher SSS in the northeastern Atlantic Ocean (cf. Figure 4).

[63] The additional SSS anomaly of 0.55 in the Weddell Sea in Experiment G2 reinstalls deep convection in the southern Weddell Sea (Figure 13), such that the temperature of AABW and the density contrast between NADW and AABW are similar to Experiment M. Finally, the additional SSS anomaly of 1.0 in Experiment G2 yields a very cold and salty AABW, colder than -1°C and even slightly saltier than the NADW; the density contrast between both water

Table 3. Implied Water Flux, its Divergence, and the Sea-Surface Salinity (SSS) in the Inner Weddell Sea (South of 63.9°S)^a

Characteristic	M	G0	G1	G2	G3
Water flux, m a^{-1}	-0.061	0.315	0.233	0.006	-0.639
Water divergence, mSv	-4.87	19.29	14.31	0.37	-39.14
SSS	34.35	35.56	35.48	35.94	36.30

^aThe implied water flux approximates the net sea-ice formation or freezing rate in the ocean model.

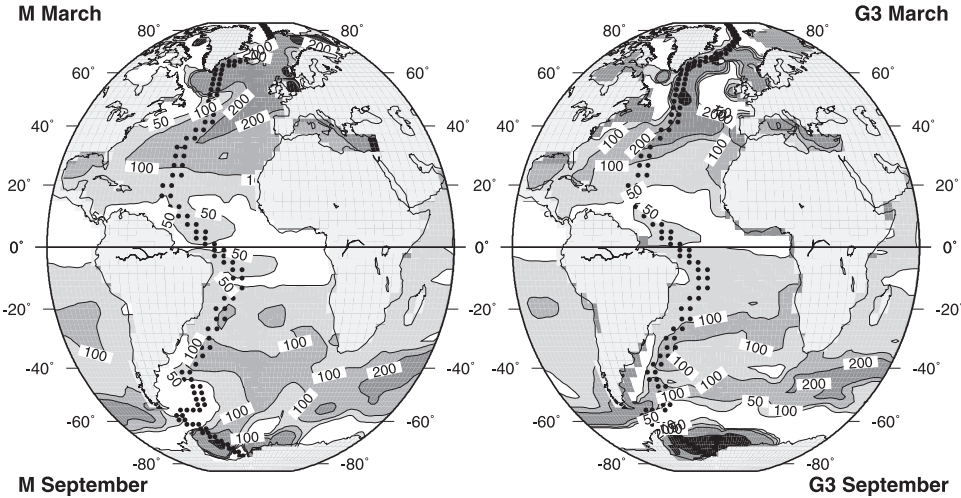


Figure 7. Mixed layer depth in the winter hemisphere, computed according to Large *et al.* [1997]. Contours are at 50, 100, and 200 m. Values larger than 300 m are colored black. (left) Modern (Experiment M). (right) Glacial (Experiment G3). Dots indicate the model grid points chosen for the west Atlantic section averages.

masses increases to 0.6 kg m^{-3} . Common to the three glacial experiments that employ the reconstructed SSS is a very cold and fresh ABW that fills the Arctic Basin north of the Greenland-Iceland-Scotland ridge and is almost isolated from the south. All four glacial experiments show a correspondingly colder ($3\text{--}4^\circ\text{C}$) and more pronounced AAIW tongue that can be traced as far as 10°N (Figure 13).

[64] In going from Experiments G0 and G1 (that are driven by identical SSS in the South Atlantic Ocean) to Experiment G3, the formation area of southern ocean deep and bottom waters migrates from the northern rim of the Weddell Sea (G0/G1) to the coast of Antarctica (G3). At the same time, their formation rate increases and their temperature decreases: The deep and bottom waters are warmer in Experiments G0 and G1 than in Experiment M, slightly colder in Experiment G2 and much (between 1 and 1.5°C) colder in Experiment G3. Increasing the additional salinity anomaly in the Weddell Sea directly affects the temperature of AABW, such that the deep and bottom water temperatures in Experiments M and G2 are very similar (see Figure 12), and that the entire deep Atlantic Ocean is near the freezing point of surface seawater in Experiment G3, in accordance with the paleoceanographic reconstruction by Adkins *et al.* [2002].

[65] The corresponding salinity distributions (Figure 14) of the glacial experiments differ from the temperature distributions in that the deep ocean salinity does not monotonously vary with the additional Weddell Sea salinity anomaly. As already discussed, the deep and bottom waters of Experiments G0 and G1 comprise a mixture of water formed in the Southern Ocean with saltier water of northern origin, and salinities below a depth of 2000 m are relatively high. The salinity anomaly of 0.55 in Experiment G2 causes the formation of AABW to shift to the southern Weddell Sea. Despite the additional anomaly, the sea surface salinity in this region is lower than in the northern North Atlantic Ocean and therefore Experiment G2 develops lower deep

and bottom water salinities than Experiment G1. The further enhancement of the additional salinity anomaly in Experiment G3 increases the deep and bottom water salinity to the values of Experiment G1 or slightly above. In all glacial salinity sections, the lower boundary of NADW is less well defined and the salinity below 2000 m depth is much more homogeneous than in Experiment M. Also common to all glacial experiments is a strong imprint of Mediterranean Outflow Water (MOW) on the salinity of upper NADW, as reconstructed by Zahn *et al.* [1987].

3.4. Meridional and Horizontal Volume Transports

[66] The meridional volume transports of the Atlantic and Indo-Pacific Oceans are quite similar in Experiments M and G1–G3. Thus we find that with at least seasonally ice-free Nordic Seas there is the possibility of ongoing NADW production at roughly the same rate as today. In Experiment M (Figure 15, Table 4), 10 Sv of new NADW are formed in the northern North Atlantic Ocean, almost 4 of which originate from the Arctic Ocean. Only 1 Sv upwells north of 30°N and 1 Sv upwells at the equator, leaving 8 Sv for export across 30°S . Of this export, 2–3 Sv then upwell in the Indo-Pacific Ocean, the remaining 5–6 Sv in the Southern Ocean. Experiment G3 shows slightly lower total rates of NADW formation (9 Sv) and upwelling in the North Atlantic Ocean as Experiment M, but the formation region is shifted to the south. About half of the NADW is formed at convection sites south of 48°N , the rest sinks at or slightly north of the Greenland-Iceland-Scotland ridge. In both Experiment M and Experiment G3, the transport of AABW amounts to 4 Sv at 30°S . Reflecting the reduced AABW formation owing to lower Weddell Sea salinities, Experiments G1 and G2 (not shown) yield lower AABW transports of 2 and 3 Sv, but higher NADW exports of 10 and 9 Sv (Table 4). We note that in the Indo-Pacific Ocean, the inflow of AABW amounts to 4 Sv in Experiment M and increases to 6 Sv in Experiment G3, with only little or no upwelling at the equator.

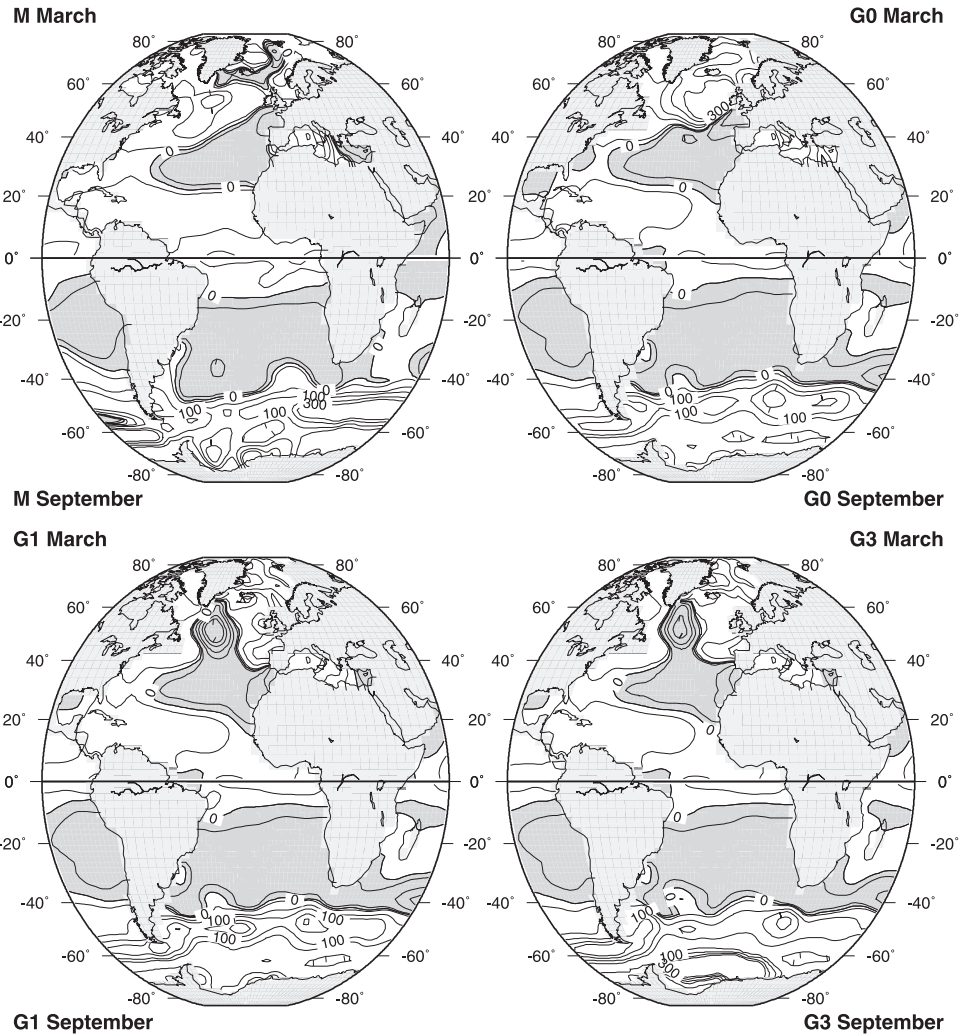


Figure 8. Barrier layer thickness (difference between isothermal and isopycnal mixed layer depth, m) in the winter hemisphere. Negative values are shaded; isolines are drawn at 0, ± 5 , ± 10 , ± 50 , ± 100 , ± 200 , and ± 300 m.

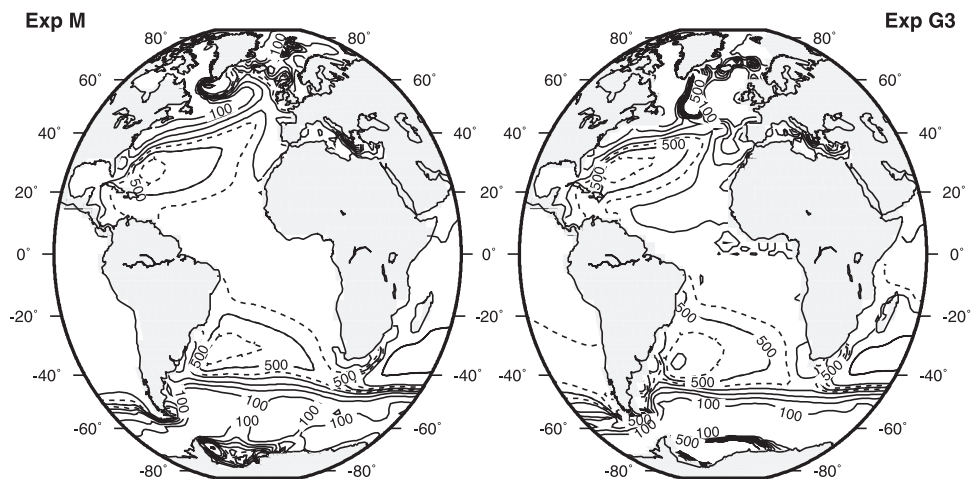


Figure 9. Maximum depth of the annual mean ventilated thermocline (m). The contour interval is 100 m, additional lines are drawn at 450 and 550 m depth (dashed) (left) Modern (Experiment M, $\sigma_0 = 26.9$ kg m $^{-3}$ isopycnal surface). (right) Glacial (Experiment G3, $\sigma_0 = 28.2$ kg m $^{-3}$ isopycnal surface).

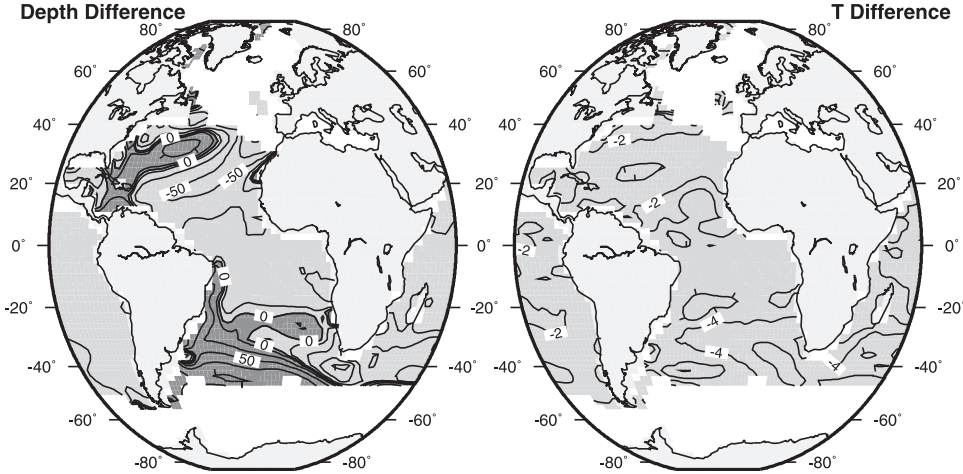


Figure 10. Differences in annual mean ventilated thermocline depth. (left) Contours at 0, ± 5 , ± 20 , ± 50 , ± 100 , and ± 200 m and temperature. (right) Contour interval 1°C between Experiment G3 and Experiment M. Light gray denotes negative; darker shade indicates positive differences.

[67] In the North Atlantic Ocean, there is a wind-driven subtropical overturning cell (the “reverse conveyor” of Seidov *et al.* [1996]) that expands and strengthens in Experiment G3 with respect to M from 1 to 2 Sv. The total northward transport of heat associated with the meridional overturning circulation is only slightly lower in Experiment G3 than in Experiment M (not shown). At 48°N, it is reduced by 0.1 PW or 20%.

[68] A comparison of Experiments G0 and M shows that the lower glacial SST alone leads to an enhanced sea-surface density gradient in the North Atlantic Ocean (Figure 5) that drives a stronger meridional overturning, similar to the findings of Schmittner *et al.* [2002]. At the same time, the AABW inflow is reduced to 2 Sv in the Atlantic Ocean and nearly vanishes in the Indo-Pacific Ocean. Experiment G0 in combination with Experiment G1 reveals that the reconstructed changes in North Atlantic SSS imply much lower densities between the Bay of Biscay and the Norwegian Sea, which act to reduce the meridional overturning.

[69] The surface water transported across Drake Passage by the additional northward Ekman drift, caused by stronger glacial westerlies, amounts to 8 Sv (not shown). This water sinks south of 50°S and flows back into the Southern Ocean below the crests of the topographic ridges that span the latitudes of Drake Passage.

[70] In our experiments, the transports of the Gulf Stream and within the northern subpolar gyre increase during the LGM by roughly 50% with respect to today (Table 4). The transport of the Brazil Current is almost the same as at present, and the Agulhas Current is weaker by about 25%. The Weddell Sea Gyre appears to be more sluggish during the LGM. However, the imposed Weddell Sea SSS anomaly accelerates the Antarctic Circumpolar Current (ACC) to almost 150% of its modern transport in Experiment G3. With increasing ACC strength, the leakage of Indian Ocean waters from the Agulhas Current into the Atlantic Ocean diminishes: In Experiment G3, it amounts to only one-third of that found in Experiment M. This is clearly reflected by

the depth and temperature changes within the ventilated thermocline (Figure 10) that is shallower and colder in the southeastern Atlantic Ocean in Experiment G3, and the transports and temperatures in the vicinity of Cape of Good Hope (Figure 11).

4. Discussion

4.1. Sea-Surface and Bottom Boundary Conditions

[71] The global mean cooling at the sea surface as implied by the GLAMAP reconstruction is about 1.2°C. This is smaller than in the CLIMAP reconstruction because of the higher SST in the subtropical to polar North Atlantic Ocean. Especially in the northeastern North Atlantic Ocean, the GLAMAP SST is still much lower than today (Figure 2, top). Taken by itself, this difference of more than 10°C would cause a large increase of the local sea-surface density at the LGM. However, owing to the low $\delta^{18}\text{O}_\text{c}$ values measured in this area, and further north along the Norwegian coast, the reconstructed salinity anomaly turns out to be quite low (Figure 2, bottom left), which counteracts the effect of the low SST. In fact, the density increase between Ireland and the Bay of Biscay is lower than westward of this region (Figure 4), where a tongue of high salinity is reconstructed along 30–40°W, quite similar to the findings of Duplessy *et al.* [1991].

[72] Between 45°S and 50°S in the South Atlantic Ocean, the reconstructed SST is about 2–4°C lower than in the modern ocean, in part owing to the more northerly position of the winter ice edge. This lower SST is the reason for the strong cooling of AAIW, which sinks in this region (Figure 13). A similar anomaly can be seen in the path of the Benguela Current way into the eastern equatorial Atlantic Ocean. Here the reconstructed SST is lower by up to 7°C in August and 5°C in February, in general accordance with Mix *et al.* [1999]. In addition, there is a strong cooling in the upwelling areas off the coasts of Northwest and Southwest Africa. The SST in the subtropical gyres is

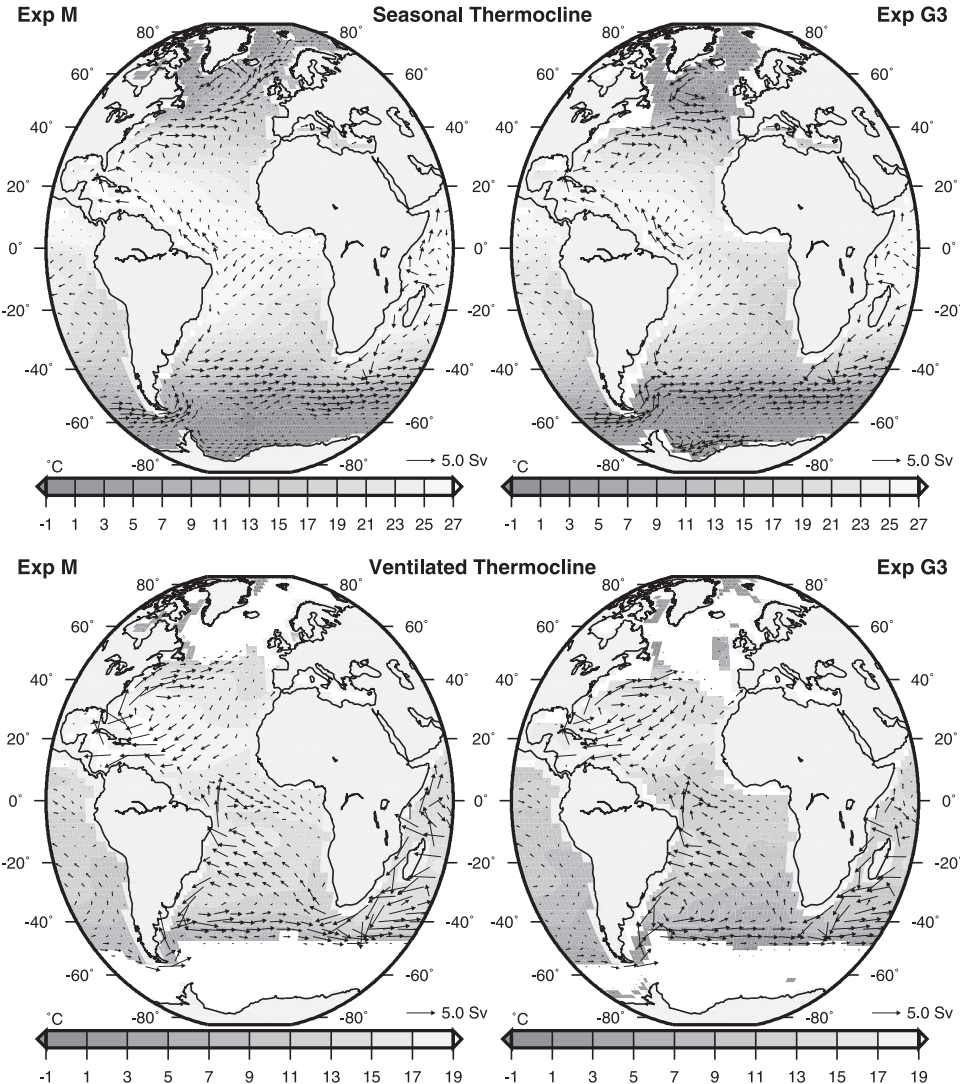


Figure 11. Annual mean horizontal circulation and temperature, vertically averaged over the (top) seasonal thermocline and the (bottom) ventilated thermocline. The lower boundary of the seasonal thermocline is defined as the annual maximum of mixed layer depth. It is at the same time the upper boundary of the ventilated thermocline. The maximum depth of the ventilated thermocline is shown in Figure 9. For clarity we show only every second vector, and arrow lengths are truncated to that of the vector which is longer than 90% of all vectors. (left) Modern (Experiment M). (right) Glacial (Experiment G3). See color version of this figure at back of this issue.

relatively unchanged compared to the modern, as was already inferred by *CLIMAP Project Members* [1981].

[73] Of the 143 sediment core sites that we used for the SSS reconstruction, most are located in the North Atlantic Ocean north of 45°N. We therefore consider the sea-surface salinity in the North Atlantic Ocean to be better constrained than in the Southern Ocean. Regions that according to the reconstructed sea-ice edges were affected by summer melting (and possibly as well by a reduction in evaporation and a southward shift of the North Atlantic storm track; cf. *Ganopolski and Rahmstorf* [2001]) show a consistently low sea-surface salinity increase, lower than the global anomaly.

[74] Depending on the particular glacial experiment, the Weddell Sea SSS anomaly either reflects the global value of 1.07 or goes beyond this value by additional shifts of 0.55 [*Duplessy et al.*, 1996] or 1.0, simulating enhanced winter sea ice formation. Our results suggest that SSS anomalies in this region are crucially important for the deep ocean T and S characteristics and for the balance of the water masses formed in northern and southern high latitudes. This can already be anticipated from the resulting sea-surface density shown in Figure 4 for Experiment G3: With the 1.0 anomaly, the Weddell Sea density is about as high as the density in the northern North Atlantic Ocean.

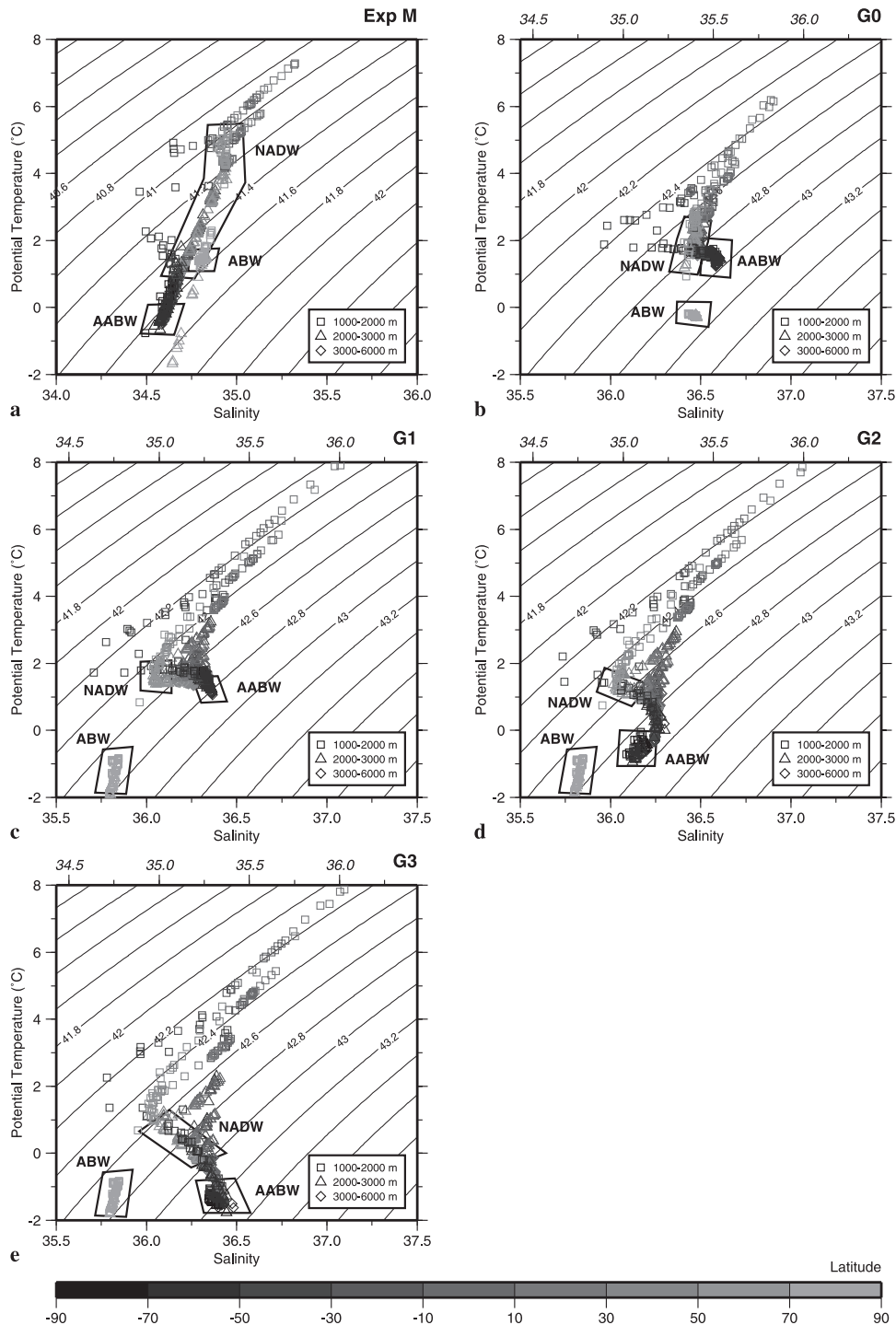


Figure 12. T-S diagrams for the western Atlantic Trough. The depth ranges 1000–2000 m, 2000–3000 m, and 3000–6000 m are indicated by different symbols. Colors represent latitude; isolines represent potential density referenced to 3000 m depth (σ_3 , kg m^{-3}). (a) Experiment M. (b) Experiment G0. (c) Experiment G1. (d) Experiment G2. (e) Experiment G3. Note the different salinity and σ_3 ranges; for comparison with Figure 14, salinity is shown at the top edge of the glacial diagrams without the global 1.07 anomaly (slanted numbers). See color version of this figure at back of this issue.

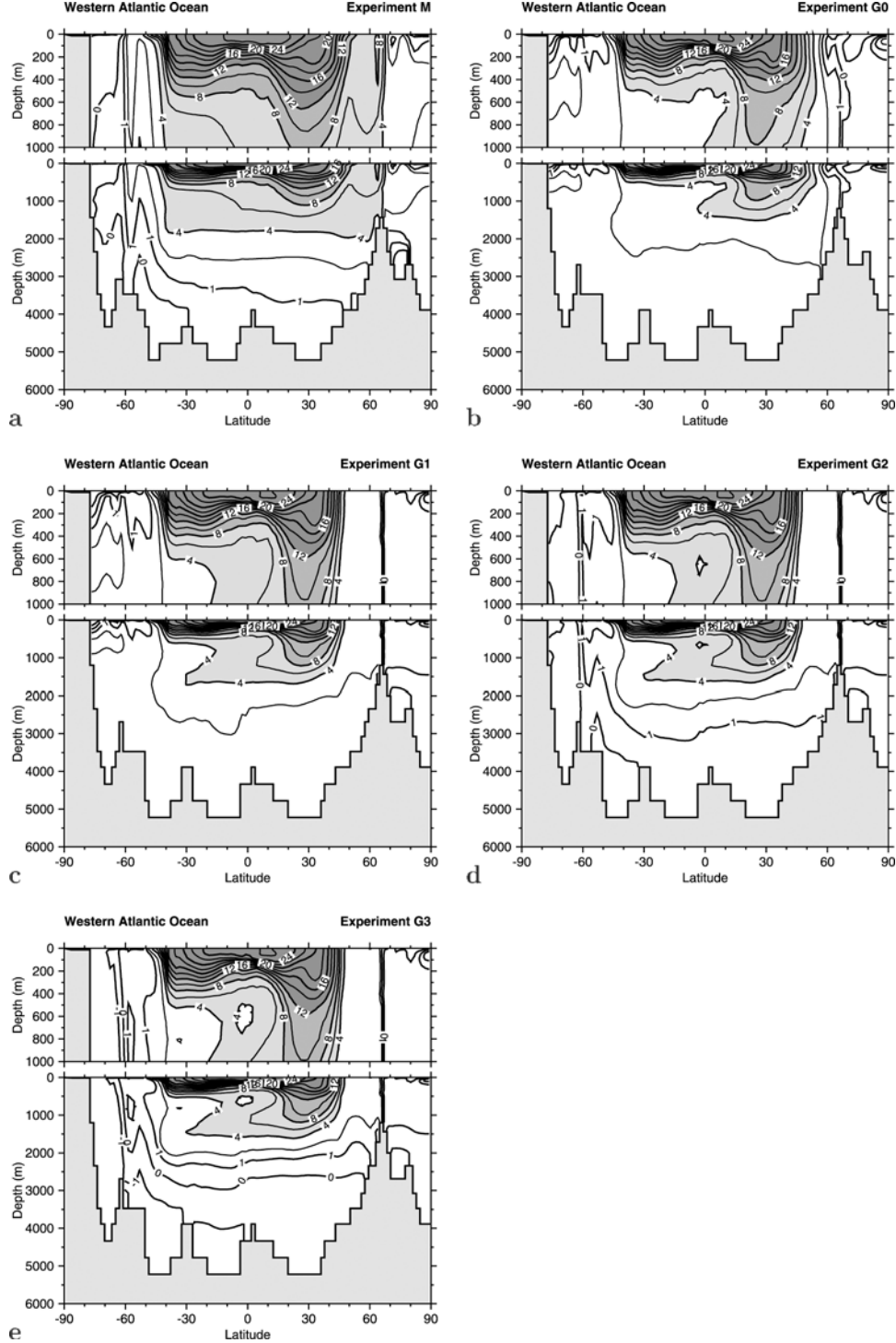


Figure 13. Annual mean potential temperature distribution along the western Atlantic Ocean transect. The contour interval is 1°C below 2°C and 2°C above. (a) Experiment M. (b) Experiment G0. (c) Experiment G1. (d) Experiment G2. (e) Experiment G3.

[75] The glacial winds are generally stronger than the modern ones (Figure 2, bottom right), and they are shifted in latitude as well (Figure 3). In the Southern Hemisphere, the location where the zonal wind stress component τ_x vanishes and the wind stress curl changes sign moves

southward by one grid row or about 3° . The maximum of the zonal wind stress component is also displaced to the south by approximately 2° . Consequently, the South Atlantic Current and the Antarctic Circumpolar Current are shifted southward. At the latitude of Cape Horn (which in

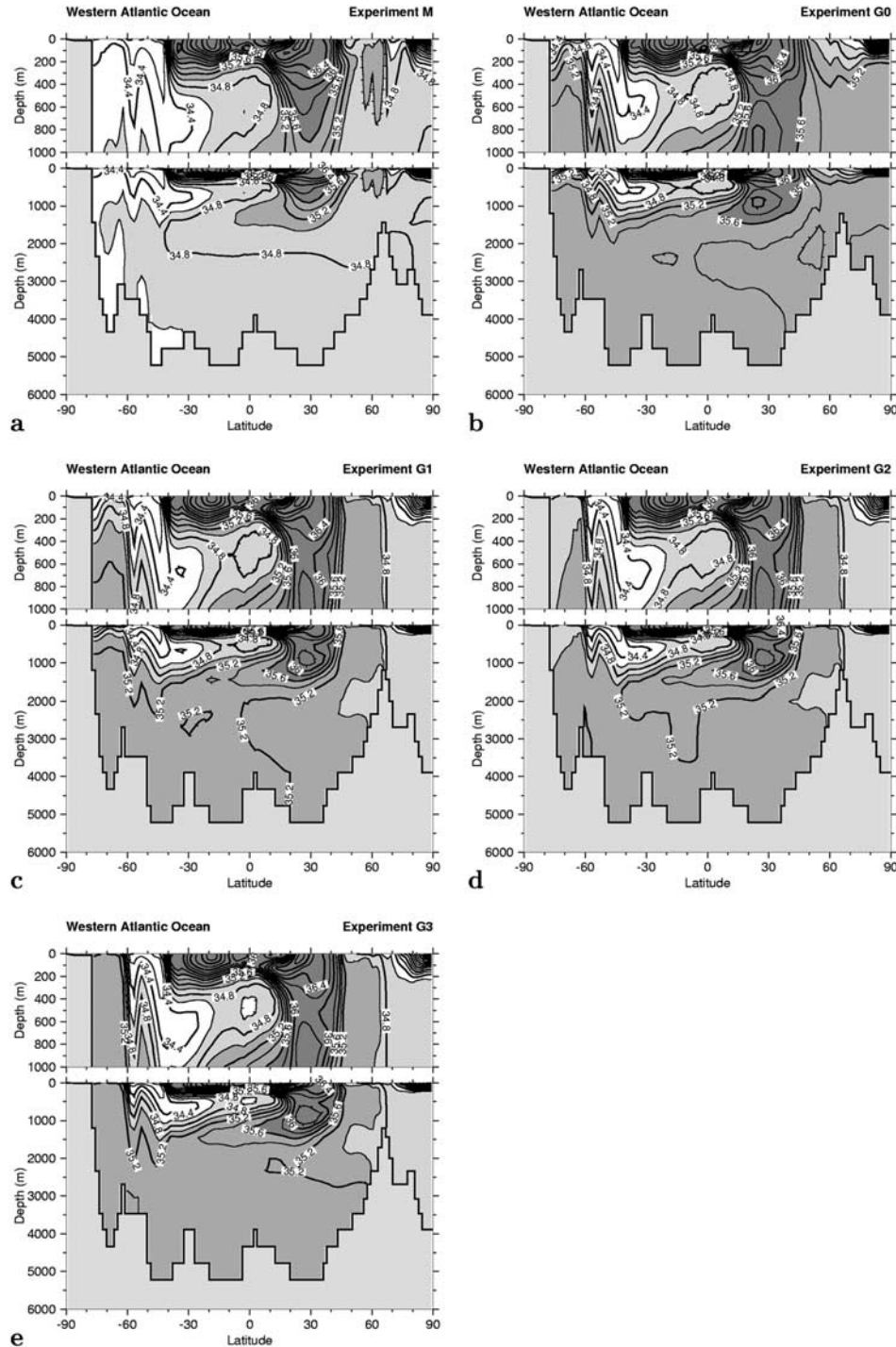


Figure 14. Annual mean salinity distribution along the western Atlantic Ocean transect. The contour interval is 0.2. (a) Experiment M. (b) Experiment G0. (c) Experiment G1. (d) Experiment G2. (e) Experiment G3. To facilitate comparison, the global 1.07 salinity anomaly was subtracted from the glacial sections.

our ocean model is 54.47°S), the wind stress is higher by 0.046 Pa or 34%. This corresponds to an increase of the zonally integrated northward Ekman transport across Drake Passage by 8 Sv.

[76] Because of the low sea level, numerous shelf regions are exposed at the LGM. These additional land areas are present in our glacial model topography in the North Sea, the Barents and Laptev Seas, along the Newfoundland and

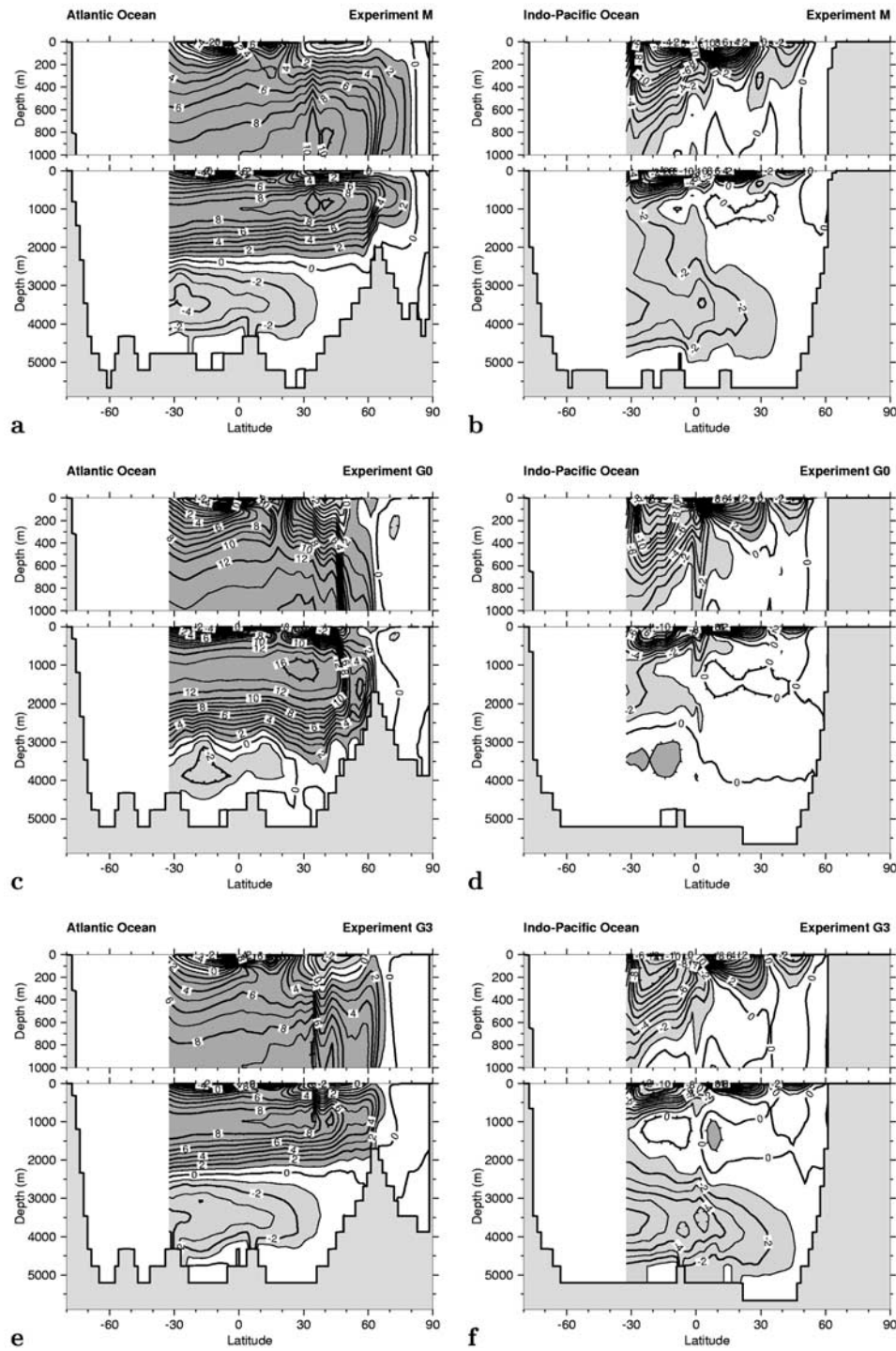


Figure 15. Annual mean meridional overturning stream function. The contour interval is 1 Sv. Positive contour levels (dark shading) indicate clockwise circulation, negative contour levels (light shading) indicate anticlockwise circulation. (a) Atlantic Ocean, Experiment M. (b) Indo-Pacific Ocean, Experiment M. (c) Atlantic Ocean, Experiment G0. (d) Indo-Pacific Ocean, Experiment G0. (e) Atlantic Ocean, Experiment G3. (f) Indo-Pacific Ocean, Experiment G3.

Table 4. Major Meridional and Horizontal Transports in Sv Simulated in the Ocean Model

Water Mass, Current	M	G0	G1	G2	G3
NADW (production)	10	16	10	10	9
NADW (outflow at 30°S)	8	14	10	9	8
AABW (inflow at 30°S)	4	2	2	3	4
Northern subpolar gyre	16.9	20.3	25.8	24.8	24.3
Gulf Stream	21.4	32.5	27.7	28.1	28.3
Brazil Current	32.6	31.4	32.5	34.2	36.2
Akulhas Current	62.3	48.6	46.5	48.2	48.9
Akulhas leakage	11.7	12.1	12.1	8.6	4.4
ACC	120.7	115.5	123.0	138.0	176.3
Weddell Sea gyre	19.1	11.4	12.2	14.3	10.3

Argentine coasts, along the Antarctic Peninsula, at Cape of Good Hope, and at the southwest and northwest African Shelves. Denmark Strait and Walvis Ridge are both shallower than today.

4.2. Thermocline Circulation

[77] *Slowey and Curry* [1995] estimate from large $\delta^{18}\text{O}$ increases in benthic foraminifera on the margins of Little Bahama Bank and Great Bahama Bank that in the North Atlantic subtropical gyre during the LGM, waters throughout the thermocline were about 4°C cooler than today and the underlying intermediate-depth waters were 2°C cooler. Their cores originate from depths between 425 and 1534 m and thus span the entire main thermocline and extend into the upper NADW. Together with further evidence from intermediate depths [*Boyle and Keigwin*, 1987], they show that the entire upper water column of the North Atlantic Ocean had more positive $\delta^{13}\text{C}$ and was depleted in nutrients during the LGM, while deep waters had more negative $\delta^{13}\text{C}$ and were enriched in nutrients. For the last glacial, *Slowey and Curry* [1995] find no minimum of $\delta^{13}\text{C}$ that today occurs at the depth of a poorly ventilated oxygen-minimum zone, near the base of the main thermocline.

[78] These changes in temperature and nutrient content are consistent with stronger winds and lower wintertime SST. According to the GLAMAP reconstruction of the glacial sea-surface temperature, large areas of the subtropical ocean were colder during winter by 2–10°C in the North Atlantic Ocean and 2–4°C in the South Atlantic Ocean. As compared to the present, all isotherms had migrated equatorward. In our model, the outcrop locations of the thermocline isopycnal surfaces in the North Atlantic Ocean shifted from about 40°–55°N in Experiment M to about 35°–45°N in Experiments G1–G3 (Figure 8). As a net result, the thermocline waters cooled by 2–3°C in the North Atlantic Ocean and 4–5°C in the South Atlantic Ocean (Figure 10). If the southward shift of the outcrop locations by 5°–10° is correctly simulated, this suggests that the subtropical GLAMAP SST is about 1–2°C too warm. In fact, a gridding technique based on objective rather than subjective interpolation yields SST values that are 1–2°C lower in this region [*Schäfer-Neth and Paul*, 2003].

[79] On the basis of their profile of benthic foraminiferal $\delta^{18}\text{O}_\text{c}$, *Slowey and Curry* [1995] also suggest that the base of the glacial thermocline was about 50–100 m shallower than today. In our model, the ventilated thermocline is up to 50 m shallower over a wide area of the subtropical

North Atlantic Ocean. No shoaling is discernible near the western boundary at the latitude of the Bahamas, which might be an artifact of the coarse zonal resolution of our ocean model. However, we note that the western boundary might be governed by different dynamics and respond differently to climate change than the interior of the subtropical gyre.

[80] The easiest and most likely explanation for increasing the oxygen content and the benthic foraminiferal $\delta^{13}\text{C}$ is a better ventilation and an increase in the flow rates of water along the isopycnals from their outcrop region in the northeast Atlantic Ocean into the main thermocline, a finding that is readily supported by our model results (Figure 11).

[81] Water of Mediterranean origin is another potential influence on the base of the thermocline. In our glacial experiments G1–G3, a stronger influence of the Mediterranean outflow below 650 m depth led to a warming of up to 1°C relative to Experiment M. This is in contrast with the benthic foraminiferal $\delta^{18}\text{O}$ from these depths by *Slowey and Curry* [1995], which indicates that our model possibly overestimates the change in the outflow. The glacial vertical temperature gradient was similar to today throughout the ventilated thermocline and in the deep and bottom waters, but differed at the base of the thermocline (650–1200 m, Figure 5), also caused by the stronger Mediterranean outflow.

[82] With the exception of the too weak gyres in the North Atlantic Ocean, the horizontal mass transports of Experiment M (Table 4) agree reasonably well with the observed current strengths [e.g., *England and Garçon*, 1994]. The large cooling in the South Atlantic Ocean in Experiment G3 is due to a change in the contributions of the two sources of the thermocline water: The Agulhas leakage is reduced and less thermocline-to-intermediate water slips from the Indian Ocean along the southern rim of the African continent into the South Atlantic Ocean (Figure 11). At the same time, more and colder water that originates from the confluence region of the Brazil and Malvinas currents is subducted into the thermocline. This is reflected in the deeper thermocline near the southern Subtropical Front and the shallower thermocline to the south of Cape of Good Hope (Figure 10).

4.3. Deep-Water Circulation

[83] As a major change from the former CLIMAP SST reconstruction, the new GLAMAP data are marked by higher temperatures in the subpolar North Atlantic Ocean and seasonally ice-free Nordic Seas. In conjunction with the available $\delta^{18}\text{O}_\text{c}$ measurements, these SSTs yield higher sea surface salinity values. This is already the case for the moderate GEOSECS SSS- $\delta^{18}\text{O}_\text{w}$ slopes we employ in this study and would be even more so for steeper slopes. Except for the Bay of Biscay with its low $\delta^{18}\text{O}_\text{c}$ values, the ice-free Nordic Seas thus imply a high sea-surface density over most of the subpolar and polar North Atlantic Ocean and cause deep convection and the formation of a relatively dense NADW. According to the results of Experiment G1, this denser deep water tends to dominate the water mass characteristic of the whole deep Atlantic Ocean (Figures 13 and 14), which is not supported by available proxy data. Hence in this experiment the bottom water in the Atlantic

Ocean has a temperature of 1° – 2°C and is warmer than in Experiment M. However, *Schrag et al.* [1996] and *Mackensen et al.* [2001] propose Atlantic bottom water masses near the freezing point. For example, *Mackensen et al.* [2001] report a glacial reduction of bottom water temperatures by 1.1 – 1.9°C at their deepest and southernmost study sites (between 44°S and 47°S and 3.8 and 4.7 km depth). To accomplish this, the denser glacial NADW must have had its counterpart in the Southern Ocean, that is, an even denser AABW. Since AABW cannot cool below the freezing point, it must have been saltier than today to balance the higher density of NADW, a conclusion first drawn by *Zahn and Mix* [1991] from oxygen isotopes of benthic foraminiferal shells. A possible mechanism to achieve the proposed salinity increase would be an intensified winter sea-ice formation in the southern Weddell Sea with its associated salt rejection and brine release. An extended winter sea-ice coverage could also ensue the formation of deep water at the northern rim of the Weddell Sea. The SSS anomaly pattern put forth by *Melles* [1991] and *Duplessy et al.* [1996] indeed suggests increased formation of sea ice in the Weddell Sea, its advection to the north and melting at the polar front. We mimicked these processes by including additional Weddell Sea salinity anomalies in Experiments G2 and G3 and found (at least in Experiment G3) the deep and very cold water mass suggested by *Schrag et al.* [1996], *Mackensen et al.* [2001] and *Adkins et al.* [2002].

4.4. Weddell Sea Freshwater Budget

[84] The net annual ice export from the inner Weddell Sea south of 63°S has been estimated to be 50 ± 19 mSv [*Harms et al.*, 2001] by a twenty-year deployment of upward looking sonar systems and satellite microwave measurements. *Timmermann et al.* [2001] use these data to validate their coupled sea ice-ocean model that yields an export of 42 ± 25 mSv. According to this model, the freshwater loss owing to sea-ice formation roughly balances ice-shelf basal melting and net precipitation and amounts to 5 ± 13 mSv in the annual mean. In our case, the net freshwater loss through the surface of the inner Weddell Sea may be inferred from the implied salinity fluxes owing to the SSS restoring boundary condition. For Experiment M, we find nearly 4.9 mSv (Table 3), which is in good agreement with the results of *Timmermann et al.* [2001]. However, it should be kept in mind that the available observations are the residuum of several large terms of different signs, namely snowfall/precipitation, glacial melt from the ice shelves and ice advection, which easily exceed the net freezing rate by an order of magnitude. This is even more the case for the seasonal variations and clearly evidenced by the large error margin of the 5 ± 13 mSv estimate given by these authors.

[85] As *Timmermann et al.* [2001] conclude, sea-ice formation appears to be a necessary condition for the renewal of AABW, and any changes in the Weddell Sea freshwater budget have a significant effect on the global circulation, a result that is also born out by our series of glacial experiments (G1–G3). As can be seen from Table 3, there is a net freshening of the Weddell Sea in Experiments G0–G2. Owing to the upwelling of salty NADW, the restoring to lower SSS implies a net melting of sea ice

instead of sea-ice formation. Only in Experiment G3, the net freshwater flux is negative again, indicating the net formation of sea ice in the inner Weddell Sea, at a rate vastly increased with respect to our control run. This nonlinear dependence of ice formation on the Weddell Sea sea-surface salinity indicates that between G2 and G3 a threshold is passed, triggering additional convection and the onset of freezing.

[86] We note that the glacial melt from the ice shelves was not necessarily larger during the LGM. Around 21 ka BP the global ice volume, as measured by deep-sea core $\delta^{18}\text{O}$ [*Waelbroeck et al.*, 2002] and inferred from observational data for sea level change [*Lambeck et al.*, 2002], reached a maximum. As a consequence, the net annual mass balance (snowfall minus melt) of all ice sheets and glaciers worldwide was nearly zero for this period. For Antarctica in particular, *Pollard and Thompson* [1997] using the GENESIS GCM predict a net surface budget at the LGM that is slightly less than their model's present-day value, owing to slightly less precipitation, as might be expected from the reduced global hydrological cycle compared to the present. Thus we think that the glacial melt was at most as large as today or maybe even smaller. A smaller glacial melt term would be in favor of a salinity increase at the Antarctic coast and support the higher freezing rate diagnosed from Experiment G3.

4.5. Evidence From $\delta^{13}\text{C}$ and ^{14}C

[87] The different strengths of AABW transport in Experiments G1–G3 can be explained by the increasing density contrast between NADW and AABW: The different sea-surface density (Figure 5) in the source area of AABW is advected into the interior and determines the meridional density gradient at depth, which in turn controls the bottom water transport [*Kamenkovich and Goodman*, 2000]. Correspondingly, the bottom water transport at 30°S amounts to 2, 3, and 4 Sv in Experiments G1, G2, and G3 (Table 4). A relatively larger contribution of water from the Southern Hemisphere as compared to that from the Northern Hemisphere at the LGM is indicated by low $\delta^{13}\text{C}$ values below 2500 m depth between 20° and 45°N , as reconstructed by, e.g., *Duplessy et al.* [1988], *Labeyrie et al.* [1992] and *Sarnthein et al.* [1994].

[88] The deep overturning circulation in the North Atlantic Ocean is particularly sensitive to the subpolar sea-surface density gradient [cf. *Gnanadesikan*, 1999; *Vallis*, 2000]. Accordingly, the stronger subpolar gradient in the glacial experiments accounts for a more intense NADW formation south of the Greenland-Iceland-Scotland ridge. In total, the glacial NADW formation is about the same as the modern (Figure 15), because in Experiment M, the NADW receives an additional contribution from north of the ridge, as indicated by the third, polar sea-surface density gradient (Figure 5).

[89] *Schäfer-Neth and Paul* [2001] describe an experiment on the basis of the temperature reconstruction by *Weinelt et al.* [1996] with also seasonally ice-free Nordic Seas and employing the same $\delta^{18}\text{O}_\text{c}$ database and a similar $\delta^{18}\text{O}_\text{w}$ -SSS relation as in our present study. Coupled off line to a global carbon-cycle box model (Experiment “LGMW”

in *Schulz and Paul* [2003]; see also *Matthies et al.* [2003] for a coupling to the Hamburg Ocean Carbon Cycle Model), this model run was used to investigate the effect of high-latitude ice cover on the marine carbon cycle, specifically the latitude- and depth-dependent $\delta^{13}\text{C}$ signal. Compared to a case with CLIMAP ice cover (Experiment “LGMC”), a better representation of the reconstructed glacial $\delta^{13}\text{C}$ distribution was found in Experiment LGMW. Although the glacial sea surface temperatures after *Weinelt et al.* [1996] are somewhat lower than the GLAMAP reconstruction, the resulting sea surface salinity and density are also higher than with the CLIMAP SSTs. As a result, the North Atlantic Ocean deep water formation area is shifted northward with respect to CLIMAP, and the water on the southern flank of the Greenland-Iceland-Scotland ridge is still ventilated from the north, which compares favorably with the eastern North Atlantic Ocean $\delta^{13}\text{C}$ data. In our experiments with ice-free Nordic Seas, roughly half of the NADW is formed at convection sites south of 48°N where the overturning reaches only 1500 m depth (Figure 15) and the convection depth is limited to 1000–1200 m (Figure 7); the rest still sinks at or even north of the ridge. We suppose that this meridional circulation would yield similar distributions of $\delta^{13}\text{C}$ and ^{14}C ages as Experiment LGMW of *Schulz and Paul* [2003].

4.6. The “Reconfigured Conveyor Belt”

[90] In contrast to previous modeling studies of the glacial ocean, we use low vertical diffusion in the upper 2000 m and a relatively high vertical resolution, which yields a realistic representation of modern Antarctic Intermediate Water. In Experiment M, the associated salinity minimum in the Atlantic Ocean can be traced as far as 10°N , is 750 m deep at 40°N and gradually rises until it reaches a depth of 500 m (Figure 14). Furthermore, the low vertical diffusion yields very little upwelling of deep water into the tropical thermocline in all experiments. Thus in the Atlantic Ocean the transport of NADW across 30°S is only 1–2 Sv lower than across 30°N , and in the Pacific Ocean most of the AABW inflow is returned at intermediate depth (Figure 15). In this respect, the meridional circulation resembles the “reconfigured conveyor belt” of *Toggweiler and Samuels* [1995b] with most of the deep water upwelling in the Southern Ocean. This “reconfigured conveyor belt” is a prerequisite for the glacial ocean as envisioned by *Keeling and Stephens* [2001], as well as a salty and cold AABW that fills a large fraction of the volume of the Atlantic Ocean. However, we do not find evidence for the other prerequisites in our glacial experiments: We do not obtain a salty AAIW; in the glacial experiments the salinity contrast between AAIW on the one hand and NADW and AABW on the other hand is even larger than in the modern experiment. In the southwestern South Atlantic Ocean where the intermediate and mode waters are formed, the surface buoyancy flux is reduced during Southern Hemisphere winter and there is even a change from positive to negative values (Figure 6). There is a band of positive sea-surface buoyancy flux that extends from the northern rim of the additional Weddell Sea SSS anomaly to the winter ice edge. This might indicate that the additional Weddell Sea

SSS anomaly should extend further northward to follow the seasonal migration of the sea-ice margin and make the sea-surface buoyancy flux negative everywhere underneath the ice. However, to really test the hypothesis for salty AAIW formation put forth by *Keeling and Stephens* [2001], an active sea-ice model for the simulation of sea-ice formation during winter and sea-ice melting during summer would be required.

[91] Owing to the changed SSTs in the Southern Ocean, the polar front is shifted southward by 2° , as born out by the sea-surface density distributions (Figure 5) and the zonal wind stress (Figure 3), thereby further increasing the glacial-to-modern difference of the maximum zonal wind stress at Drake Passage (0.04 Pa) by 20%. However, the “Drake Passage effect” (as originally proposed by *Toggweiler and Samuels* [1995b]), is not enhanced under glacial sea-surface boundary conditions: The additional Ekman drift of 8 Sv owing to the stronger glacial wind stress does not feed into the northward moving water masses of the upper Atlantic Ocean and finally into the NADW formation. Instead, the water sinks at the polar front to a depth below the crests of the topographic ridges and flows back into the Southern Ocean in the so-called Deacon cell. Presumably, this is because the wind stress does not increase in isolation, but along with a cooling of the SST, associated with a weakening of the stratification north of Drake Passage. The “Deacon-cell shortcut” has been found before in an ocean model coupled to a simple atmosphere model [*Rahmstorf and England*, 1997], in which wind stress and SST change in concert, too.

4.7. Sea-Surface Restoring Versus Coupled Ocean-Atmosphere Models

[92] Our results are based on an ocean-only model run under restoring boundary conditions on sea-surface temperature and salinity. On the one side, compared to coupled ocean-atmosphere models, we thereby lose a set of independent information for model validation because we spend it on model forcing. On the other side, we gain sea-surface conditions as close to the paleoreconstructions as possible which at present cannot be achieved by coupled climate models. Thus we infer the ocean circulation and distribution of water masses from the available proxy data. Our sea-surface conditions for temperature and salinity need not to be physically consistent, but to some degree the model results can point out the discrepancies and yield estimates of paleoceanographic parameters for regions that have not yet been extensively studied.

[93] We note that traditional restoring boundary conditions have a drawback: If the ocean model perfectly reproduces the imposed SST and SSS, it will have zero heat and freshwater fluxes, which is clearly wrong. Usually, the simulation ends up with a compromise with errors in both, the SST and SSS fields as well as the implied heat and freshwater fluxes. In our control experiment, surface fields such as the mixed layer density, subsurface fields such as the density and depth of the ventilated thermocline, and the water mass characteristics as evident from the T-S diagrams, appear to be rather realistic. Since the modern buoyancy flux (Figure 6) corresponds well to the present-day obser-

vations by *Schmitt et al.* [1989], we think that a reasonable balance between errors in the SST and SSS fields on the one hand and in the fluxes on the other hand is achieved.

[94] We used the densely spaced SST and SSS reconstructions for the North Atlantic Ocean as a starting point. Then, the assessment of our series of three glacial experiments with respect to independently reconstructed deep-sea temperatures [*Schrag et al.*, 1996; *Mackensen et al.*, 2001] not only suggests a glacial Weddell Sea salinity increase that is in qualitative agreement with the sparse Southern Ocean sediment cores, but it gives as well a quantitative estimate of more than 0.55, possibly even close to 1 for this anomaly.

[95] In Experiments G0–G3, the subpolar sea-surface density gradient (Figure 5) occurs over a smaller and more southern range of latitudes than in Experiment M, which reflects the southward shift as well as the more zonal path of the glacial Gulf Stream and North Atlantic Drift. This glacial pattern and the still active although reduced exchange of water masses between the northeastern Atlantic Ocean and the Nordic Seas are both in accordance with the results of *Hewitt et al.* [2001]. In their coupled model study of the LGM, they find slightly higher SSTs over some regions of the North Atlantic Ocean. The meridional circulation intensifies and in the midlatitudes more heat is transported by the strong subpolar gyre circulation; some weak convection takes place in the Norwegian Sea. The southward return flow from the Nordic Seas is across the Iceland-Scotland Ridge and not through the Denmark Strait. This is in agreement with our results, however, we must note that our horizontal resolution is not sufficient for a realistic representation of the currents through these narrow channels.

[96] In the NCAR CCSM [*Shin et al.*, 2003], the tropics show a glacial cooling of 3°C over land and 2°C over the ocean; thus SSTs are about 1°C lower than CLIMAP, which at least for August applies to the GLAMAP SSTs as well. The meridional overturning circulation in the Atlantic Ocean shows a moderate decrease by about 20% in the formation of NADW and a slight increase in the inflow of AABW, which is accompanied by a shoaling of the NADW cell. The glacial-to-modern change in zonal wind stress is remarkably similar to the ECHAM3 response to the monthly GLAMAP SST fields (Figure 3): In the Southern Ocean, the wind stress is increased by about 25% and its maximum is shifted poleward by 3°–4°. *Shin et al.* [2003] attribute the deep circulation changes to the increased surface density flux in the Southern Ocean caused by sea-ice expansion in their LGM simulation. Most important in this connection is the large Weddell Sea salinity anomaly of about 1.5, excluding the global salinity increase of 1. This salinity anomaly under sea ice is mainly due to the release of brine during winter sea-ice formation and the subsequent sea-ice export to lower latitudes. A large positive SSS anomaly is also found to the south of Greenland, but it is due to a decrease in the difference between precipitation and evaporation (*P-E*). Between this area of higher SSS and Ireland, salinities are decreased with respect to the global anomaly, a pattern that is clearly present in our SSS reconstructions based on oxygen isotopes. In fact, except for the sea ice-covered

regions, there is a general decrease in SSS by 0.5–1.0 owing to an overall increase in *P-E*.

[97] To further assess the magnitude of the SSS anomaly in the Weddell Sea, we ran two sensitivity experiments with the University of Victoria (UVic) coupled climate model. This model consists of the MOM 2 ocean model in a configuration similar to ours, coupled to an atmospheric energy-moisture balance model and a sea-ice model with a simple zero layer formulation of thermodynamics and viscous-plastic dynamics [*Weaver et al.*, 2001]. As boundary conditions for a glacial sensitivity experiment we imposed the orbital parameters of 21,000 a BP and an atmospheric CO₂ concentration of 200 ppm. As a result, the Weddell Sea SSS anomaly between the glacial sensitivity experiment and the modern control experiment also turned out to be positive near the Antarctic coast and at the northern rim of the Weddell Sea to the east of the Antarctic Peninsula, where it reached up to 0.4–0.5 throughout the year. Thus our estimated Weddell Sea salinity is well within the range indicated by two different coupled climate models.

5. Conclusions

[98] For the first time we could exploit the synoptic sea-surface conditions that have been reconstructed over the past decade by three different research groups for the North and South Atlantic Oceans as well as the Atlantic sector of the Southern Ocean at the LGM. These reconstructions of glacial ice cover and SST, as well as our estimates of glacial SSS, are comparable to those available from comprehensive coupled models. Thus we are confident that our results can contribute to the emerging picture of the stratification of the ocean “at the cold end of climate variations,” closely tied to the proxy data from ocean sediment cores.

[99] With its high vertical resolution, low vertical diffusion and isopycnal mixing, our ocean model realistically reproduced the circulation of the thermocline and intermediate waters, controlled by the subtropical and subpolar sea-surface density gradients, as well as the characteristics of the deep ocean, set by the interhemispheric sea-surface density balance between the northern North Atlantic Ocean and the Weddell Sea. In particular, the low vertical diffusion of only 0.1 cm² s⁻¹ in the upper 2000 m allowed for very low rates of upwelling from the deep ocean into the tropical thermocline and thus a more intact conveyor belt. Together with the isopycnal mixing parameterization, which is of great importance for the subduction of water into the thermocline and its transport along the isopycnal surfaces, we achieved a better representation of the subsurface flow field than in many previous modeling studies.

[100] According to our model simulations, during the LGM the ventilated thermocline was cooler than today by 2–3°C in the north and 4–5°C in the South Atlantic Ocean. Its depth was reduced by 50 m on average, namely in the tropics. In the North Atlantic Ocean, the outcrop locations of the thermocline isopycnal surfaces migrated southward by 5°–10°, and the ventilation increased. As for the glacial South Atlantic Ocean, the ventilated thermocline deepened

to the east of Cape Horn and shoaled to the southwest of Cape of Good Hope. As a consequence, the mixed layer and thermocline water masses were dominated by cold water originating near Drake Passage, and transports of warm water from the Indian Ocean into the Atlantic Ocean were reduced to about 40% of their modern value. AAIW was colder by 3–4°C, NADW by 2.5°C and AABW by 1°C.

[101] The meridional overturning rates of NADW and AABW in the Atlantic Ocean turned out to be similar to today. With regard to the water mass exchange between the northeastern Atlantic Ocean and the Nordic Seas, we found that warm currents did extend northward into the Greenland and Norwegian Seas, albeit at a much reduced strength. In this vein, ice-free Nordic Seas during glacial times could allow for some deep convection and overturning north of the Greenland-Iceland-Scotland ridge and deep ventilation at its southern flank, which would be consistent with the $\delta^{13}\text{C}$ data from fossil benthic foraminiferal shells.

[102] Given the high density implied by the GLAMAP SST reconstruction for the surface of the northern North Atlantic Ocean, the evidence for a relatively larger contribution of AABW as compared to NADW at depth and the reconstructed cooling of AABW constrain the possible range of glacial sea-surface salinity in the sparsely sam-

pled Southern Ocean. In our model, only a local sea-surface salinity anomaly of about 1 beyond the global anomaly implied net sea-ice formation in the inner Weddell Sea and raised the sea-surface density in this region above the level in the northern North Atlantic Ocean. This led to the formation of a very cold (close to the freezing point) and salty AABW, even slightly saltier than the NADW. If the sea-surface density of the Southern Ocean were to fall below that of the northern North Atlantic Ocean, deep convection in the Southern Ocean would cease, no Antarctic Bottom Water would be formed and the deep and bottom water would warm as compared to the modern case. Such a scenario would clearly be in conflict with the glacial-to-Holocene changes in $\delta^{13}\text{C}$ data and ^{14}C ages.

[103] **Acknowledgments.** We thank Anne de Vernal for making her LGM SST and sea-ice reconstructions available to us, Gerrit Lohmann and Stefan Lorenz for running the ECHAM3 atmospheric general circulation model, and Andreas Manschke for his continued technical support. We highly appreciate the many suggestions and comments by Michael Schulz on the final draft of our manuscript. Finally, we are grateful to Gavin Schmidt and an anonymous referee for their very constructive reviews. This research was funded by the Deutsche Forschungsgemeinschaft (DFG) as part of the DFG Research Center “Ocean Margins” of the University of Bremen, RCOM 0044.

References

- Abelmann, A., U. Brathauer, R. Gersonde, R. Sieger, and U. Zielinski, Radiolarian-based transfer function for the estimation of sea surface temperatures in the Southern Ocean (Atlantic sector), *Paleoceanography*, **14**, 410–421, 1999.
- Adkins, J. F., K. McIntyre, and D. P. Schrag, The salinity, temperature, and $\delta^{18}\text{O}$ of the glacial deep ocean, *Science*, **298**, 1769–1773, 2002.
- Bard, E., M. Arnold, P. Maurice, J. Duprat, and J.-C. Duplessy, Retreat velocity of the North Atlantic polar front during the last deglaciation determined by ^{14}C accelerator mass spectrometry, *Nature*, **328**, 791–794, 1987.
- Bemis, B. E., H. J. Spero, J. Bijma, and D. W. Lea, Reevaluation of the oxygen isotopic composition of planktonic foraminifera: Experimental results and revised paleotemperature equations, *Paleoceanography*, **13**, 150–160, 1998.
- Bigg, G. R., An ocean general circulation model view of the glacial Mediterranean thermohaline circulation, *Paleoceanography*, **9**, 705–722, 1994.
- Bigg, G. R., and E. R. Rohling, An oxygen isotope data set for marine water, *J. Geophys. Res.*, **105**, 8527–8535, 2000.
- Bigg, G. R., M. R. Wadley, D. P. Stevens, and J. A. Johnson, Simulations of two last glacial maximum ocean states, *Paleoceanography*, **13**, 340–351, 1998.
- Boyle, E. A., and L. Keigwin, North Atlantic thermohaline circulation during the last 20,000 years: Link to high-latitude surface temperature, *Nature*, **330**, 35–40, 1987.
- Bryan, K., and L. J. Lewis, A water mass model of the world ocean circulation, *J. Geophys. Res.*, **84**, 2503–2517, 1979.
- CLIMAP Project Members, Seasonal reconstructions of the Earth’s surface at the Last Glacial Maximum, *Geol. Soc. Am. Map Chart Ser.*, MC-36, pp. 1–18, Geol. Soc. Am., Boulder, Colo., 1981.
- De Vernal, A., C. Hillaire-Marcel, J.-L. Turon, and J. Matthesen, Reconstruction of sea-surface temperature, salinity and sea ice cover in the northern North Atlantic during the Last Glacial Maximum based on dinocyst assemblages, *Can. J. Earth Sci.*, **37**, 725–750, 2000.
- Deutsch, C. V., and A. G. Journel, *GSLIB: Geostatistical Software Library and User’s Guide*, Oxford Univ. Press, New York, 1992.
- De Vernal, A., C. Hillaire-Marcel, R. W. Peltier, and A. J. Weaver, Structure of the upper water column in the northwest North Atlantic: Modern versus Last Glacial Maximum conditions, *Paleoceanography*, **17**, 1–15, 2002.
- Duplessy, J.-C., N. J. Shackleton, R. G. Fairbanks, L. Labeyrie, L. Oppo, D. Kallel, and N. Kallel, Deepwater source variations during the last climatic cycle and their impact on the global deepwater circulation, *Paleoceanography*, **3**, 343–360, 1988.
- Duplessy, J.-C., L. Labeyrie, A. Juillet-Leclerc, F. Maitre, J. Duprat, and M. Sarnthein, Surface salinity reconstruction of the North Atlantic Ocean during the last glacial maximum, *Oceanol. Acta*, **14**, 311–324, 1991.
- Duplessy, J.-C., L. Labeyrie, M. Arnold, M. Paterne, J. Duprat, and T. C. E. van Weering, Changes in surface salinity of the North Atlantic during the last deglaciation, *Nature*, **358**, 485–488, 1992.
- Duplessy, J. C., L. Labeyrie, M. Paterne, S. Hovine, T. Fichefet, J. Duprat, and M. Labracherie, High latitude deep water sources during the Last Glacial Maximum and the Intensity Of The Global Oceanic Circulation, in *The South Atlantic: Present and Past Circulation*, edited by G. Wefer et al., pp. 445–460, Springer-Verlag, New York, 1996.
- England, M. H., and V. Garçon, South Atlantic circulation in a world ocean model, *Ann. Geophys.*, **12**, 812–825, 1994.
- Epstein, S., R. Buchsbaum, H. A. Lowenstam, and H. C. Urey, Revised carbonate-water isotopic temperature scale, *Geol. Soc. Am. Bull.*, **64**, 1315–1325, 1953.
- Fieg, K., and R. Gerdes, Sensitivity of the thermohaline circulation to modern and glacial surface boundary conditions, *J. Geophys. Res.*, **106**, 6853–6867, 2001.
- Ganopolski, A., and S. Rahmstorf, Rapid changes of glacial climate simulated in a coupled climate model, *Nature*, **409**, 153–158, 2001.
- Ganopolski, A., S. Rahmstorf, V. Petoukhov, and M. Claussen, Simulation of modern and glacial climates with a coupled model of intermediate complexity, *Nature*, **391**, 351–356, 1998.
- Gent, P. R., and J. C. McWilliams, Isopycnal mixing in ocean circulation models, *J. Phys. Oceanogr.*, **20**, 150–155, 1990.
- Gersonde, R., and U. Zielinski, The reconstruction of late Quaternary Antarctic sea-ice distribution—The use of diatoms as proxies for sea ice, *Palaeogeogr. Palaeoclimatol. Palaeoecol.*, **162**, 263–286, 2000.
- Gersonde, R., et al., Last glacial sea surface temperatures and sea-ice extent in the Southern Ocean (Atlantic-Indian sector): A multiproxy approach, *Paleoceanography*, **18**, doi:10.1029/2002PA000809, in press, 2003.
- Gnanadesikan, A., A global model of silicon cycling: Sensitivity to eddy parametrization and dissolution, *Global Biogeochem. Cycles*, **13**, 199–220, 1999.
- Harms, S., E. Fahrbach, and V. H. Strass, Sea ice transports in the Weddell Sea, *J. Geophys. Res.*, **106**, 9057–9073, 2001.
- Hartmann, D. L., *Global Physical Climatology*, Academic, San Diego, Calif., 1994.

- Hewitt, C. D., A. J. Broccoli, J. F. B. Mitchell, and R. J. Stouffer, A coupled model study of the last glacial maximum: Was part of the North Atlantic relatively warm?, *Geophys. Res. Lett.*, 28, 1571–1574, 2001.
- Jansen, E., and H. H. Erlenkeuser, Ocean circulation in the Norwegian Sea 15000 b.p. to present, *Boreas*, 14, 189–206, 1985.
- Jansen, E., and T. Veum, Evidence for two-step deglaciation and its impact on North Atlantic deep water circulation, *Nature*, 343, 612–616, 1990.
- Jones, G. A., and L. D. Keigwin, Evidence from FRAM Strait (78°N) for early deglaciation, *Nature*, 336, 56–59, 1989.
- Jünger, B., Tiefenwassererneuerung in der Grönlandsee während der letzten 340000 Jahre, *GEOMAR Rep.* 35, 103 pp., GEOMAR Res. Cent. for Marine Geosci., Kiel, Germany, 1993.
- Kalnay, E., et al., The NCEP/NCAR reanalysis project, *Bull. Am. Meteorol. Soc.*, 77, 437–471, 1996.
- Kamenkovich, I. V., and P. J. Goodman, The dependence of AABW transport in the Atlantic on vertical diffusivity, *Geophys. Res. Lett.*, 27, 3739–3742, 2000.
- Keeling, R. F., and B. B. Stephens, Antarctic sea ice and the control of pleistocene climate instability, *Paleoceanography*, 16, 112–131, 2001.
- Keigwin, L. D., and E. A. Boyle, Late Quaternary chemistry of high-latitude surface waters, *Palaeogeogr. Palaeoclimatol. Palaeoecol.*, 3, 85–106, 1989.
- Kellogg, T. B., J.-C. Duplessy, and N. N. Shackleton, Planctonic foraminiferal and oxygen isotopic stratigraphy and paleoclimatology of Norwegian deep-sea cores, *Boreas*, 7, 61–73, 1978.
- Kitoh, A., S. Murakami, and H. Koide, A simulation of the last glacial maximum with a coupled atmosphere-ocean GCM, *Geophys. Res. Lett.*, 28, 2221–2224, 2001.
- Köhler, S. E. I., Spätquartäre paläo-ozeanographische Entwicklung des Nordpolarmeers anhand von Sauerstoff- und Kohlenstoffisotopenverhältnissen der planktischen Foraminifere Neogloboquadrina pachyderma (sin.), *GEOMAR Rep.*, 13, 104 pp., GEOMAR Res. Cent. for Marine Geosci., Kiel, Germany, 1991.
- Labeyrie, L. D., J.-C. Duplessy, J. Duprat, A. Juillet-Leclerc, J. Moyes, E. Michel, N. Kallel, and N. J. Shackleton, Changes in the vertical structure of the North Atlantic ocean between glacial and modern times, *Quat. Sci. Rev.*, 11, 401–413, 1992.
- Lackschewitz, K. S., Sedimentationsprozesse am aktiven mittelatlantischen Kolbinsey Rücken (nördlich von Island), *GEOMAR Rep.* 9, 121 pp., GEOMAR Res. Cent. for Marine Geosci., Kiel, Germany, 1991.
- Lambeck, K., Y. Yokoyama, and T. Purcell, Into and out of the Last Glacial Maximum: Sea-level change during oxygen isotope stages 3 and 2, *Quat. Sci. Rev.*, 21, 343–360, 2002.
- Large, W. G., G. Danabasoglu, S. C. Doney, and J. C. McWilliams, Sensitivity to surface forcing and boundary layer mixing in a global ocean model: Annual-mean climatology, *J. Phys. Oceanogr.*, 27, 2418–2447, 1997.
- Lautenschlager, M., and K. Herterich, Atmospheric response to Ice Age conditions: Climatology near the Earth's surface, *J. Geophys. Res.*, 95, 22,547–22,557, 1990.
- Ledwell, J. R., A. J. Watson, and C. S. Law, Evidence for slow mixing across the pycnocline from an open-ocean tracer release experiment, *Nature*, 364, 701–703, 1993.
- Lorenz, S., B. Grieger, P. Helbig, and K. Herterich, Investigating the sensitivity of the atmospheric general circulation model ECHAM 3 to paleoclimatic boundary conditions, *Geologische Rundschau*, 86, 513–524, 1996.
- Mackensen, A., H.-W. Hubberten, N. Scheele, and R. Schlitzer, Decoupling of $\delta^{13}\text{C}_{\Sigma\text{CO}_2}$ and phosphate in recent Weddell Sea deep and bottom water: Implications for glacial Southern Ocean paleoceanography, *Paleoceanography*, 11, 203–215, 1996.
- Mackensen, A., M. Rudolph, and G. Kuhn, Late Pleistocene deep-water circulation in the subantarctic eastern Atlantic, *Global Planet. Change*, 30, 197–229, 2001.
- Marchal, O., R. François, T. F. Stocker, and F. Joos, Ocean thermohaline circulation and sedimentary $^{231}\text{Pa}/^{230}\text{Th}$ ratio, *Paleoceanography*, 15, 625–641, 2000.
- Matthies, M., T. Bickert, and A. Paul, Last glacial $\delta^{13}\text{C}$ distribution and deep-sea circulation in the Atlantic Ocean: A model-data comparison, in *The South Atlantic During the Late Quaternary: Material Budget and Current System*, edited by G. Wefer et al., Springer-Verlag, New York, in press, 2003.
- Melles, M., Late Quaternary paleoglaciology and paleoceanography at the continental margin of the southern Weddell Sea, *Antarctica, Ber. Polarforsch.*, 81, 190 pp., Alfred-Wegener-Inst. für Polar- und Meeresforsch., Bremerhaven, Germany, 1991.
- Mix, A. C., A. E. Morey, N. G. Pisias, and S. W. Hostettler, Foraminiferal faunal estimates of paleotemperature: Circumventing the no-analog problem yields cool ice age tropics, *Paleoceanography*, 14, 350–359, 1999.
- Morris, T. H., Stable isotope stratigraphy of the Arctic Ocean: Fram Strait to central Arctic, *Palaeogeogr. Palaeoclimatol. Palaeoecol.*, 64, 201–219, 1988.
- Mulitza, S., B. Donner, G. Fischer, A. Paul, J. Pätzold, and M. Segl, The South Atlantic oxygen-isotope record of planktic foraminifera, in *The South Atlantic During the Late Quaternary: Material Budget and Current Systems*, edited by G. Wefer et al., Springer-Verlag, New York, in press, 2003.
- NCAR Data Support Section, NGDCETOPO5 global ocean depth and land elevation, 5-min, *Data Set 759.1*, Natl. Cent. for Atmos. Res., Boulder, Colo., 1986.
- Niebler, H.-S., and R. Gersonde, A planktic foraminiferal transfer function for the southern South Atlantic Ocean, *Mar. Micropaleontol.*, 34, 213–234, 1998.
- Niebler, H.-S., H. W. Arz, B. Donner, S. Mulitza, J. Pätzold, and G. Wefer, Sea surface temperatures in the equatorial and South Atlantic Ocean during the Last Glacial Maximum (23–19 ka), *Paleoceanography*, 18, doi:10.1029/2003PA000902, in press, 2003.
- Östlund, H., H. Craig, W. S. Broecker, and D. Spencer, *GEOSECS Atlantic, Pacific, and Indian Ocean Expeditions: Shorebased Data and Graphics*, GEOSECS Atlas Series, vol. 7, U.S. Gov. Print. Off., Washington, D. C., 1987.
- Pacanowski, R. C. E., *MOM 2: Documentation, User's Guide and Reference Manual*, Tech. Rep. 3.2, GFDL Ocean Group, Geophys. Fluid Dyn. Lab., Princeton, N. J., 1996.
- Paleoclimate Modelling Intercomparison Project (PMIP), Paleoclimate modelling intercomparison project, *Tech. Rep.*, 1993. (Available at <http://www-pcmdi.llnl.gov/pmip/newsletters/newsletter02.html>.)
- Paul, A., S. Mulitza, J. Pätzold, and T. Wolff, Simulation of oxygen isotopes in a global ocean model, in *Use of Proxies in Paleoceanography: Examples From the South Atlantic*, edited by G. Fischer and G. Wefer, pp. 655–686, Springer-Verlag, New York, 1999.
- Peltier, W. R., Ice age paleotopography, *Science*, 265, 195–201, 1994.
- Pflaumann, U., J. Duprat, C. Pujol, and L. D. Labeyrie, SIMMAX: A modern analog technique to deduce Atlantic sea surface temperatures from planktonic foraminifera in deep sea sediments, *Paleoceanography*, 11, 15–35, 1996.
- Pflaumann, U., et al., Glacial North Atlantic: Sea surface conditions reconstructed by GLAMAP 2000, *Paleoceanography*, 18, doi:10.1029/2002PA000774, in press, 2003.
- Pollard, D., and S. L. Thompson, Climate and ice-sheet mass balance at the last glacial maximum from the GENESIS version 2 global climate model, *Quat. Sci. Rev.*, 16, 841–863, 1997.
- Prell, W. L., The stability of low latitude sea surface temperature: An evaluation of the CLIMAP reconstruction with emphasis on the positive SST anomalies, *Tech. Rep.*, Dep. of Energy, Washington, D. C., 1985.
- Rahmstorf, S., and M. H. England, Influence of Southern Hemisphere winds on north atlantic deepwater flow, *J. Phys. Oceanogr.*, 27, 2040–2055, 1997.
- Ruddiman, W. F., and A. A. McIntyre, The North Atlantic during the last deglaciation, *Palaeogeogr. Palaeoclimatol. Palaeoecol.*, 35, 145–214, 1981.
- Sarnthein, M., K. Winn, S. J. A. Jung, J.-C. Duplessy, L. Labeyrie, H. Erlenkeuser, and G. Ganssen, Changes in east Atlantic deepwater circulation over the last 30,000 years: Eight time slice reconstructions, *Paleoceanography*, 9, 209–267, 1994.
- Sarnthein, M., et al., Variations in Atlantic surface ocean paleoceanography, 50–80N: A time-slice record of the last 30,000 years, *Paleoceanography*, 10, 1063–1094, 1995.
- Sarnthein, M., R. Gersonde, S. Niebler, U. Pflaumann, R. Spielhagen, J. Thiede, G. Wefer, and M. Weinelt, Overview of Glacial Atlantic Ocean Mapping (GLAMAP 2000), *Paleoceanography*, 18(2), 1030, doi:10.1029/2002PA000769, 2003a.
- Sarnthein, M., U. Pflaumann, and M. Weinelt, Past extent of sea ice in the northern North Atlantic inferred from foraminiferal paleotemperature estimates, *Paleoceanography*, 18, doi:10.1029/2002PA000771, in press, 2003b.
- Schäfer-Neth, C., Changes in the seawater-oxygen isotope relation between last glacial and present: Sediment core data and OGCM modelling, *Paleoclimates*, 2, 101–131, 1998.
- Schäfer-Neth, C., and A. Paul, Circulation of the glacial Atlantic: A synthesis of global and regional modeling, in *The Northern North Atlantic: A Changing Environment*, edited by P. Schäfer et al., pp. 441–462, Springer-Verlag, New York, 2001.
- Schäfer-Neth, C., and A. Paul, The Atlantic Ocean at the last glacial maximum, 1: Objective mapping of the GLAMAP sea-surface conditions, in *The South Atlantic During the Late Quaternary: Material Budget and Current System*, edited by G. Wefer et al., Springer-Verlag, New York, in press, 2003.
- Schäfer-Neth, C., C. C. Hervada-Sala, V. Pawlowsky-Glahn, and K. Stattegger, Geostatistical interpretation of paleoceanographic data over large ocean basins—Reality and fiction, in *Proceed-*

- ings of the Fourth Annual Conference of the International Association for Mathematical Geology*, edited by A. Buccianti, G. Nardi, and R. Potenza, pp. 111–116, De Frede, Napoli, Italy, 1998.
- Schmidt, G. A., Error analysis of paleosalinity calculations, *Paleoceanography*, 14, 422–429, 1999.
- Schmidt, G. A., G. R. Bigg, and E. J. Rohling, Global seawater oxygen-18 database, *Tech. Rep.*, Goddard Institute for Space Studies, New York, 1999. (Available at <http://www.giss.nasa.gov/data/o18data>)
- Schmitt, R. W., P. S. Bogden, and C. S. Dorman, Evaporation minus precipitation and density fluxes in for the North Atlantic, *J. Phys. Oceanogr.*, 19, 1208–1221, 1989.
- Schmittner, A., K. J. Meissner, M. Eby, and A. J. Weaver, Forcing of the deep ocean circulation in simulations of the Last Glacial Maximum, *Paleoceanography*, 17, 26–35, 2002.
- Schrag, D. P., G. Hampt, and D. W. Murray, Pore fluid constraints on the temperature and oxygen isotopic composition of the global ocean, *Science*, 272, 1930–1932, 1996.
- Schulz, M., and A. Paul, Sensitivity of the ocean-atmosphere carbon cycle to ice-covered and ice-free conditions in the Nordic Seas during the Last Glacial Maximum, *Palaeogeogr. Palaeoclimatol. Palaeoecol.*, in press, 2003.
- Seidov, D., and B. J. Haupt, Global ocean thermohaline conveyor at present and in the late Quaternary, *Geophys. Res. Lett.*, 24, 2817–2820, 1997.
- Seidov, D., M. Sarnthein, K. Stattegger, R. Prien, and M. Weinelt, North Atlantic ocean circulation during the last glacial maximum and a subsequent meltwater event: A numerical model, *J. Geophys. Res.*, 101, 16,305–16,332, 1996.
- Shin, S.-I., Z. Liu, B. Otto-Bliesner, E. C. Brady, J. E. Kutzbach, and S. P. Harrison, A simulation of the Last Glacial Maximum climate using the NCAR-CCSM, *Clim. Dyn.*, 20, 127–151, 2003.
- Simstich, J., Die ozeanische Deckschicht des Europäischen Nordmeeres im Abbild stabiler Isotope unterschiedlicher Planktonforaminiferen, *Ber. Inst. Geowissensch.*, 32, 96 pp., Univ. of Kiel, Kiel, Germany, 1999.
- Slowey, N. C., and W. B. Curry, Glacial-interglacial differences in circulation and carbon cycling within the upper western North Atlantic, *Paleoceanography*, 10, 715–732, 1995.
- Sprintall, J., and M. Tomczak, Evidence of the barrier layer in the surface layer of the Tropics, *J. Geophys. Res.*, 97, 7305–7316, 1992.
- Timmermann, R., A. Beckmann, and H. H. Hellmer, The role of sea ice in the fresh water budget of the Weddell Sea, *Ann. Glaciol.*, 33, 419–424, 2001.
- Toggweiler, J. R., and B. Samuels, Effect of sea ice on the salinity of Antarctic bottom waters, *J. Phys. Oceanogr.*, 25, 1980–1997, 1995a.
- Toggweiler, J. R., and B. Samuels, Effect of Drake Passage on the global thermohaline circulation, *Deep Sea Res.*, 42, 477–500, 1995b.
- Tomczak, M., and J. S. Godfrey, *Regional Oceanography: An Introduction*, Pergamon, New York, 1994.
- Vallis, G. K., Large-scale circulation and production of stratification: Effects of wind, geometry, and diffusion, *J. Phys. Oceanogr.*, 30, 933–954, 2000.
- Veum, T., M. Arnold, I. Beyer, and J.-C. Duplessy, Water mass exchange between the North Atlantic and the Norwegian Sea during the last 28,000 years, *Nature*, 356, 783–785, 1992.
- Vogelsang, E., Paläo-Ozeanographie des Europäischen Nordmeers am Hand stabiler Kohlenstoff- und Sauerstoffisopen, *Ber. Sonderforsch.*, 23, 136 pp., Univ. Kiel, Kiel, Germany, 1990.
- Waelbroeck, C., L. Labeyrie, E. Michel, J. C. Duplessy, J. F. McManus, K. Lambeck, E. Balbon, and M. Labacherie, Sea-level and deep water temperature changes derived from benthic foraminiferal isotopic records, *Quat. Sci. Rev.*, 21, 295–305, 2002.
- Weaver, A. J., M. Eby, A. F. Fanning, and E. C. Wiebe, The climate of the last glacial maximum in a coupled atmosphere-ocean model, *Nature*, 394, 847–853, 1998.
- Weaver, A. J., et al., The UVic earth system climate model: Model description, climatology, and applications to past, present and future climates, *Atmos. Ocean*, 39, 361–428, 2001.
- Weinelt, M., Veränderungen der Oberflächenzirkulation im Europäischen Nordmeer während der letzten 60,000 Jahre—Hinweise aus stabilen Isotopen, *Ber. Sonderforsch.* 41, 105 pp., Univ. Kiel, Kiel, Germany, 1993.
- Weinelt, M., M. Sarnthein, U. Pflaumann, H. Schulz, S. Jung, and H. Erlenkeuser, Ice-free Nordic Seas during the Last Glacial Maximum? Potential sites of deepwater formation, *Palaeoclimates*, 1, 283–309, 1996.
- Weinelt, M., et al., Paleoceanographic proxies in the northern North Atlantic, in *The Northern North Atlantic: A Changing Environment*, edited by P. Schäfer et al., pp. 319–352, Springer-Verlag, New York, 2001.
- Winguth, A. M. E., D. Archer, J. C. Duplessy, E. Maier-Reimer, and U. Mikolajewicz, Sensitivity of paleonutrient tracer distributions and deep-sea circulation to glacial boundary conditions, *Paleoceanography*, 14, 304–323, 1999.
- World Ocean Atlas (WOA), *World Ocean Atlas 1998*, *Tech. Rep.*, Natl. Oceanogr. Data Cent., Silver Spring, Md., 1998. (Available at <http://www.nodc.noaa.gov/oc5/woa98.html>)
- Yu, E.-F., R. Francois, and M. P. Bacon, Similar rates of modern and last-glacial ocean thermohaline circulation inferred from radiochemical data, *Nature*, 379, 689–694, 1996.
- Zahn, R., and A. C. Mix, Benthic foraminiferal $\delta^{18}\text{O}$ in the ocean's temperature-salinity-density field: Constraints on the ice age thermohaline circulation, *Paleoceanography*, 6, 1–20, 1991.
- Zahn, R., B. Markussen, and J. Thiede, Stable isotope data and depositional environments in the Late Quaternary, *Nature*, 314, 433–435, 1985.
- Zahn, R., M. Sarnthein, and H. Erlenkeuser, Benthic isotope evidence for changes of the Mediterranean outflow during the late Quaternary, *Paleoceanography*, 2, 543–559, 1987.
- Zielinski, U., R. Gersonde, R. Sieger, and D. Fütterer, Quaternary surface water temperature estimations: Calibration of a diatom transfer function for the Southern Ocean, *Paleoceanography*, 13, 365–383, 1998.

A. Paul and C. Schäfer-Neth, DFG Research Center Ocean Margins and Department of Geosciences, University of Bremen, PO Box 33 04 40, D-28334 Bremen, Germany. (apau@palmmod.uni-bremen.de; csn@uni-bremen.de)

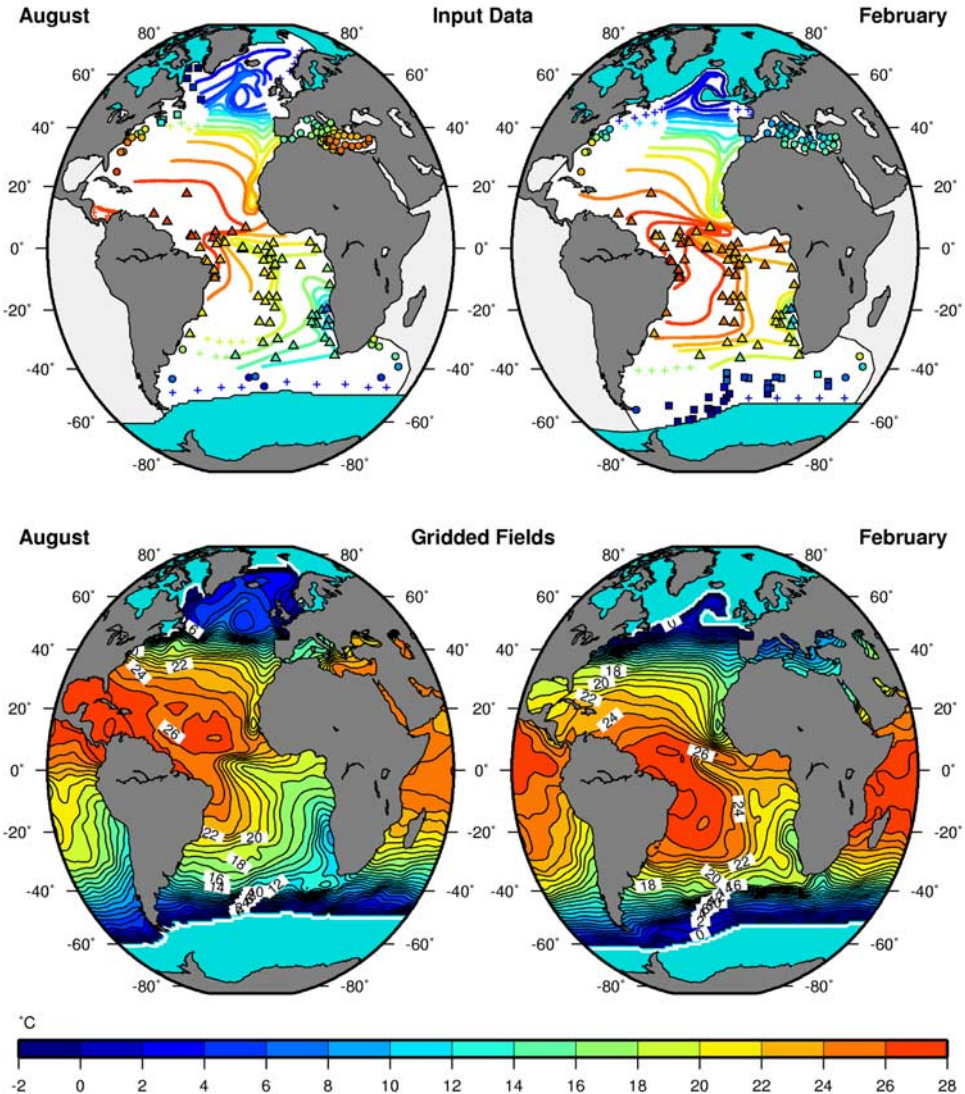


Figure 1. Glacial sea surface temperature ($^{\circ}\text{C}$). (top) Database. Isolines, Pflaumann et al. [2003]. Triangles, Niebler et al. [2003]. Squares, De Vernal et al. [2000] (August) and Gersonde et al. [2003] (February). Circles, Prell [1985] (Atlantic) and Bigg [1994] (Mediterranean). Blue (medium gray), ice cover after Pflaumann et al. [2003], De Vernal et al. [2000], and Gersonde and Zielinski [2000]. Light gray, SST data taken from CLIMAP Project Members [1981]. Pluses, artificial tie points to prevent unrealistic gradients in the interpolated fields. (bottom) Resulting $1^{\circ} \times 1^{\circ}$ gridded fields; white lines denote ice edge.

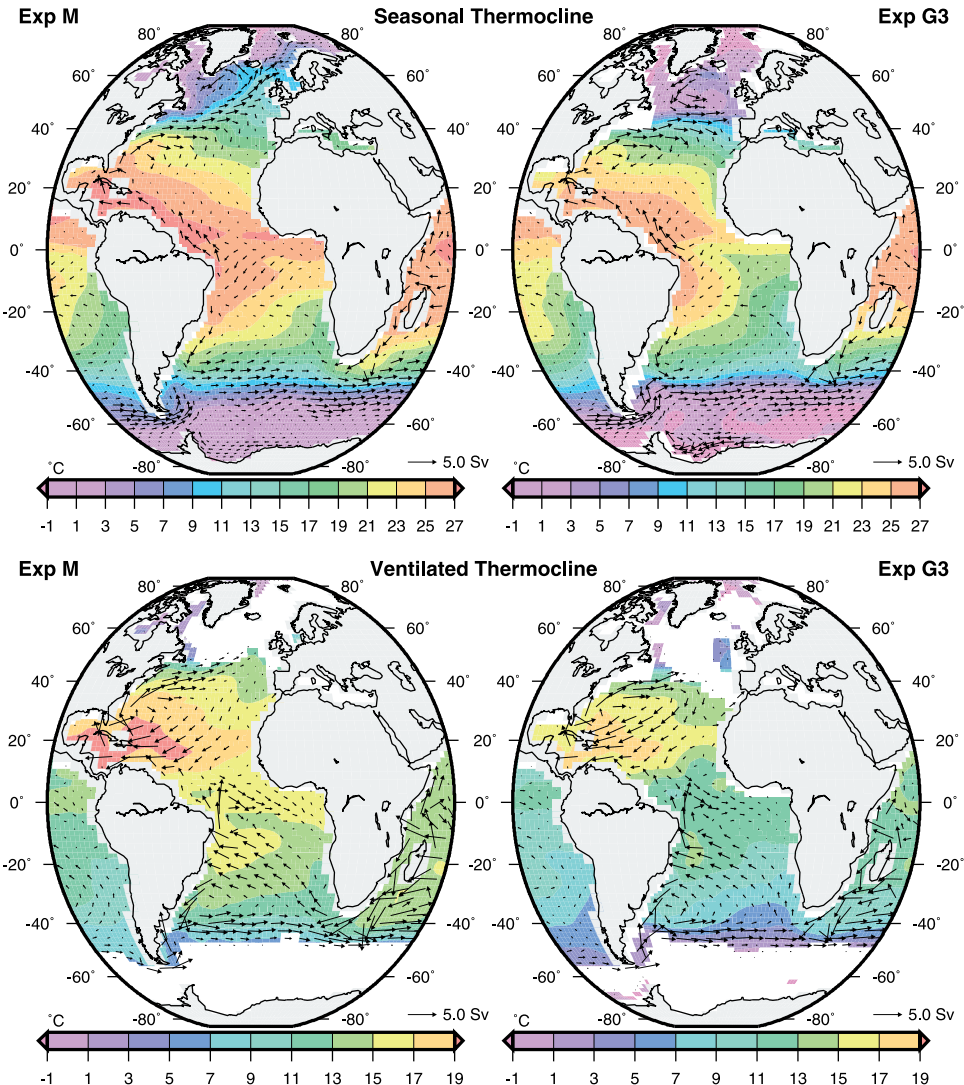


Figure 11. Annual mean horizontal circulation and temperature, vertically averaged over the (top) seasonal thermocline and the (bottom) ventilated thermocline. The lower boundary of the seasonal thermocline is defined as the annual maximum of mixed layer depth. It is at the same time the upper boundary of the ventilated thermocline. The maximum depth of the ventilated thermocline is shown in Figure 9. For clarity we show only every second vector, and arrow lengths are truncated to that of the vector which is longer than 90% of all vectors. (left) Modern (Experiment M). (right) Glacial (Experiment G3).

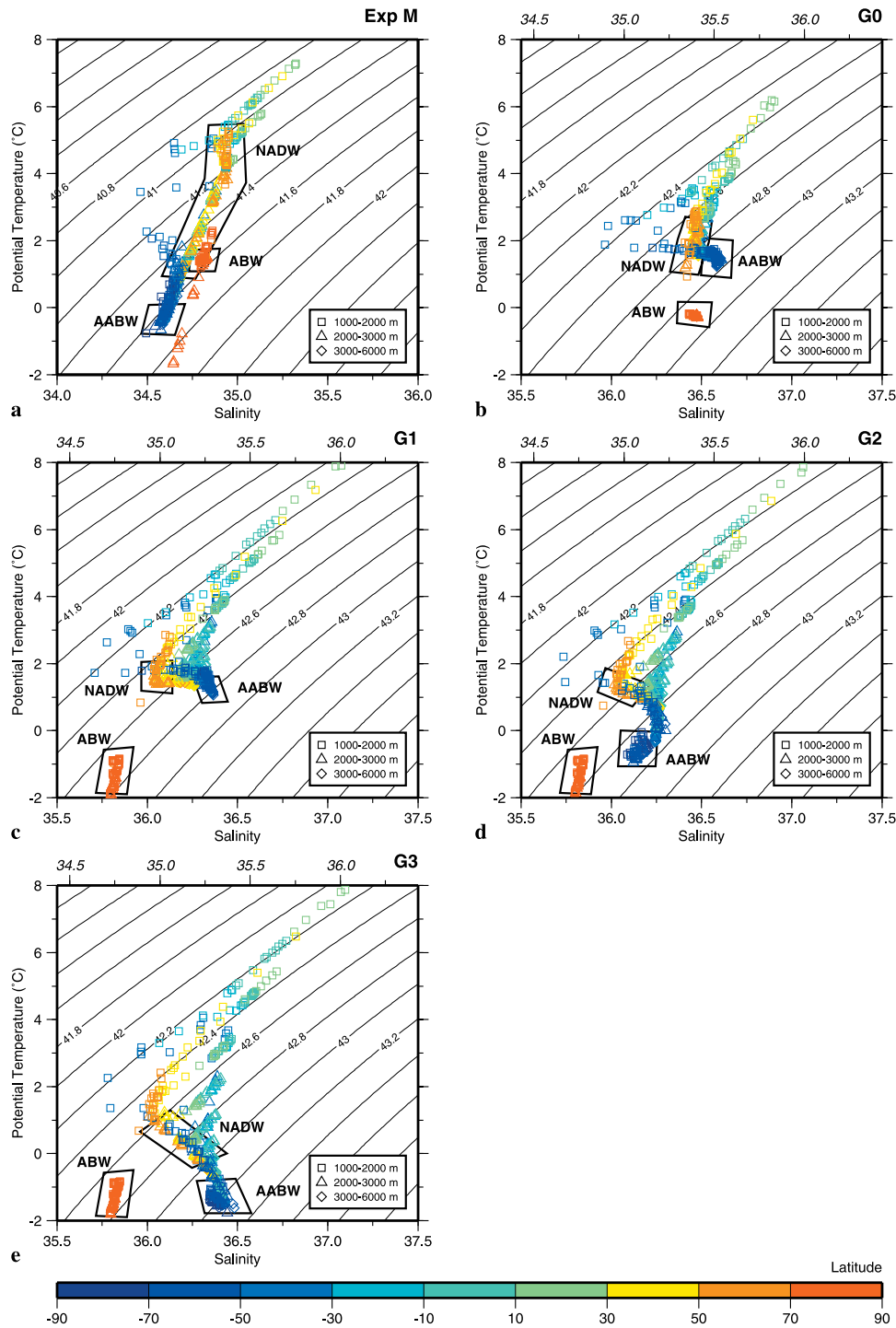


Figure 12. T-S diagrams for the western Atlantic Trough. The depth ranges 1000–2000 m, 2000–3000 m, and 3000–6000 m are indicated by different symbols. Colors represent latitude; isolines represent potential density referenced to 3000 m depth (σ_3 , kg m^{-3}). (a) Experiment M. (b) Experiment G0. (c) Experiment G1. (d) Experiment G2. (e) Experiment G3. Note the different salinity and σ_3 ranges; for comparison with Figure 14, salinity is shown at the top edge of the glacial diagrams without the global 1.07 anomaly (slanted numbers).